S
UiS

FACULTY OF SCIENCE AND TECHNOLOGY

MASTER'S THESIS

Study programme / specialisation: Petroleum Geosciences Engineering	The *spring* semester, *2023* Open
Author: Deniz Firat Seyfeli	
Supervisor at UiS: Alejandro Escalona Varela, Xiaoan Zhong	
Thesis title: Lithological Heterogeneities in the Zechstein Group: Compressed Air Energy Storage Opportunities in Salt Caverns	
Credits (ECTS): 30	
Keywords: CAES, energy storage, salt characterization, salt cavern, Zechstein Group	Pages: 70 Stavanger, *15/06/2023*

Lithological Heterogeneities in the Zechstein Group: Compressed Air Energy Storage Opportunities in Salt Caverns

by

Deniz Firat Seyfeli

Master's Thesis

Presented to the Faculty of Science and Technology

The University of Stavanger

The University of Stavanger

June 2023

Abstract

Ensuring a sustainable future necessitates the adoption of renewable energy sources, such as wind and solar energy. However, these energy sources are inherently intermittent, which emphasizes the need for effective energy storage solutions. Among the various options available, compressed air energy storage (CAES) stands out as a cost-effective and practical mechanical storage approach suitable for large-scale implementation. In this context, underground salt caverns emerge as particularly favorable sites for energy storage due to their notable impermeability, high solubility, and low contamination rates. Accordingly, the objective of this study is to identify and characterize the Upper Permian salt formations within the Zechstein Group, located in the Norwegian sector of the Southern North Sea, with the aim of proposing an optimal reservoir location for creating salt caverns for the CAES applications.

The study investigated a comprehensive collection of subsurface data, which includes a 3D seismic cube spanning an area of 3070 km^2, over 140 kilometers of 2D seismic lines, and multiple borehole data encompassing well tops, logs, reports, etc. Well data were mainly sourced from the Diskos database of the Norwegian Petroleum Directorate (NPD), which ensured the reliability and accuracy of obtained information. Industry-standard software tools such as Landmark DecisionSpace and SLB Petrel were employed for data analysis, structural interpretation, geological mapping, and 3D visualization.

Various salt structures within the Zechstein Group were successfully identified and classified. Three maps in two-way travel time (TWT) domain were generated after seismic interpretation, including the top and base Zechstein Group structural map and the thickness of the Zechstein Group. These maps aided in both spatial distribution and the geometry of salt structures. To understand the internal structures and heterogeneity of these salt structures, five facies were classified by integrating seismic amplitudes, borehole log responses, and the observation of conventional cores from nearby reference wells. Three-dimensional facies models were constructed for two selected salt diapirs. Two halite-rich facies are suggested for creating caverns in salt diapirs due to relatively homogeneous lithology within structureless or chaotic geo-bodies. Above findings from this study were ultimately utilized to propose an optimal location for the criterion of salt caverns, thereby facilitating efficient CAES operations.

Acknowledgment

Table of Contents

List of Figures

List of Tables

1. Introduction

The use of fossil fuels, causing emissions to rise globally, is a significant contributor to the climate crisis and global warming. Switching to renewable energy sources, such as wind and solar, is necessary for a sustainable future (United Nations, 2023). Nevertheless, these renewable energy sources are inconsistent and can be influenced by weather patterns, uneven energy usage, and seasonal changes (Ravestein et al., 2018; Mlilo et al., 2021). To overcome these limitations, researchers have suggested the idea of storing renewable energy (Barton and Infield, 2004; Connolly, 2012; Bocklisch, 2015; Olabi, 2017; Wang et al., 2019; Abdalla et al., 2021; Arsad et al., 2022; Kebede et al., 2022).

In the renewable energy field, various energy storage technologies exist such as electrochemical, hydrogen, thermal, and mechanical storage methods (Ould Amrouche et al., 2016). Mechanical storage includes Flywheel Energy Storage (FES), Pumped-Storage Hydropower (PSH), and Compressed Air Energy Storage (CAES) systems (Mongird et al., 2019; Fjellestad Heitmann, 2020). While batteries in electrochemical storage may be difficult to use at a large scale, mechanical storage options like the CAES are cost-effective and practical for large-scale use (DeCarolis and Keith, 2006).

Bulk energy storage can be achieved by utilizing underground geological formations such as porous rocks, depleted hydrocarbon reservoirs, and salt caverns (Succar & Williams 2008; Crotogino et al., 2017) (Figure 1). Salt caverns, in particular, are well suited for bulk energy storage. They are artificial underground cavities in salt formations, characterized by exceptional gas tightness and inertness, created by controlled injection of fresh water from the surface into the deposits (Malachowska et al., 2022). They are considered a favorable option for storing large amounts of energy because of their numerous advantages such as low investment cost, high storage capacity, low cushion gas requirement, high sealing potential, low contamination rate, high heat conduction, and resistance to chemical reactions with most of the stored substances (Caglayan et al., 2020; Geissbühler et al., 2018; Kim et al., 2012; Malachowska et al., 2022; Tarkowski, 2019). The primary challenges associated with storing energy in underground salt caverns include two folds; first of all, the collapse of the roof, which is usually due to the low height-to-diameter ratio of the cavern or the presence of a thin cap rock; and secondly, the failure of the cement casing around the wellbores, which often caused by varied densities of the rocks and the presence of

micro-fractures (Duhan, 2018; Labaune et al., 2018; Maia da Costa et al., 2019; He et al., 2022; Sadeghi et al., 2022).
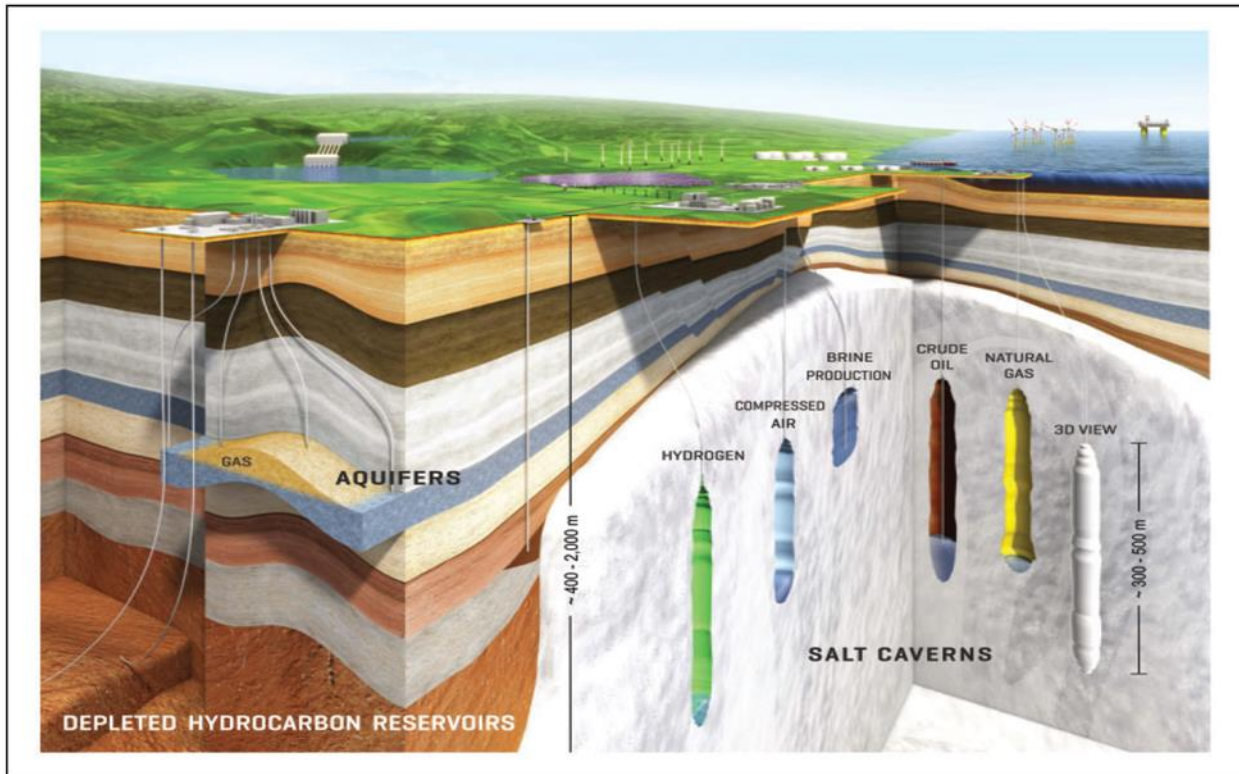
Figure 1: Overview of geological options for underground energy storage (after Crotogino et al., 2017).

Salt deposits accumulated significantly in the Permian formations on the Norwegian Continental Shelf (NCS), especially in the North Sea and Barent Sea (Gerard and Buhrig, 1990; Rossland et al., 2013; Rojo et al., 2020). The Barents Sea is home to a few salt-related basins, including the Tromsø, Nordkapp, and Tiddlybanken Basins (Rojo et al., 2019). On the other hand, the Norwegian North Sea, a vital energy center, has a large extension of salt formations. It is crucial to find geological storage solutions within these salt formations (Marin et al. 2022). Halite is the main part of these salt formations, which can provide reservoir conditions for various energy storage techniques (Parkes et al., 2018; Evans et al., 2021). Halite beds in the upper Permian Zechstein Group of the Southern North Sea represent an opportunity for future salt cavern underground energy storage and development (Marin et al. 2022). These formations typically appear as layered evaporitic sequences (LES), which may be interbedded with different evaporites, as well as carbonate, clastic, and volcanic rocks (Rowan et al., 2019; Wicker and Ford, 2021). The

Southern Norwegian North Sea is an ideal location to study the composition of the LES in the upper Permian Zechstein Group due to the abundant subsurface data readily accessible to the public (Marin et al., 2022). The subsurface deformation of LES leads to the formation of various salt structures, such as bedded salt, salt pillows, and salt diapirs (Gillhaus and Horvath, 2008; Jackson and Hudec, 2017) (Figure 2). The interpretation of these lithological heterogeneities in the different salt structures is important for choosing the optimal cavern site and minimizing drilling risk (Duffy et al., 2022).
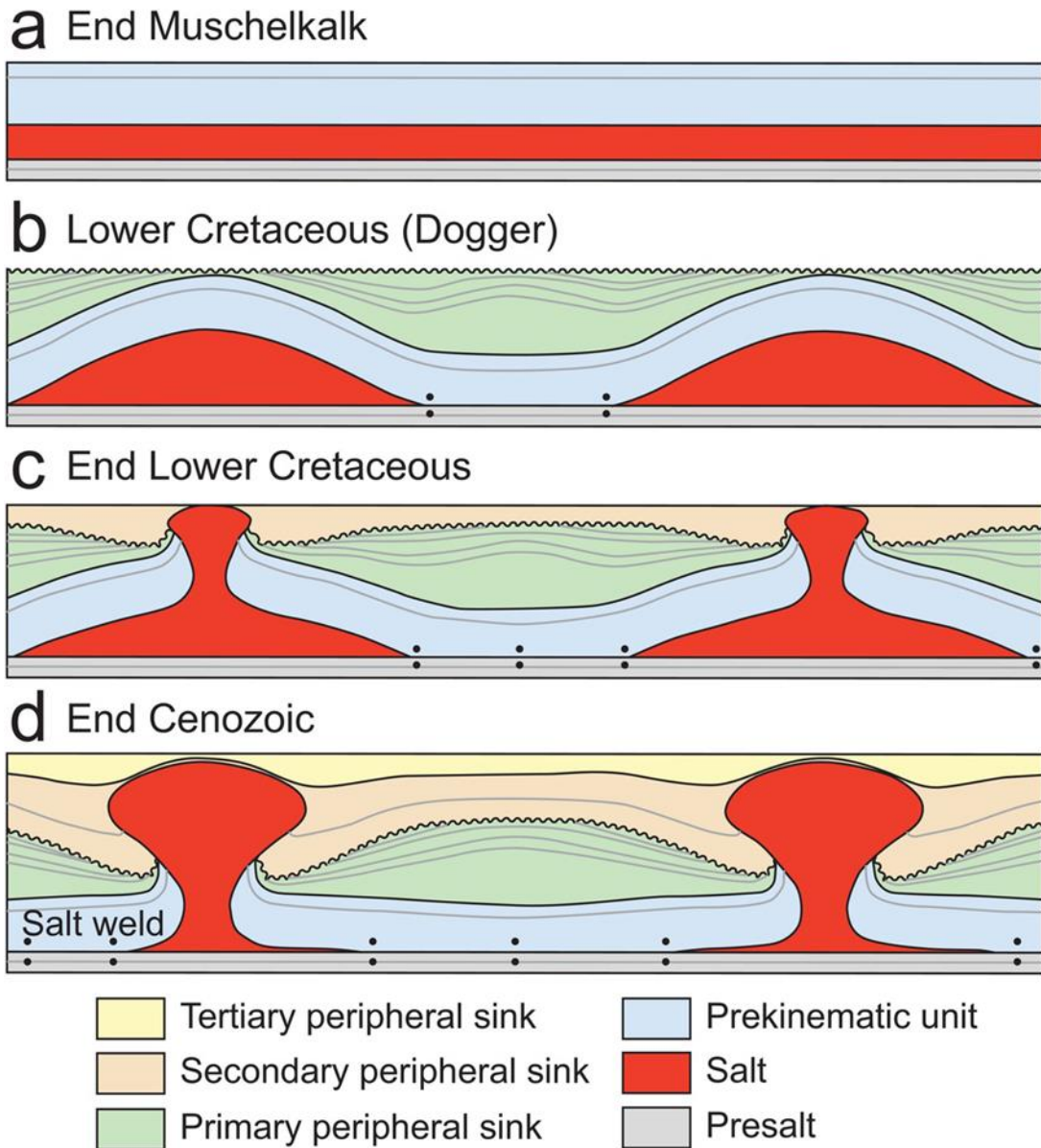
Figure 2: A bedded salt containing Permian Zechstein salt (a) evolves into a salt pillow (b), then into a salt diapir (c), and finally into a post-diapir stage (d) (after Jackson and Hudec, 2017).

Although the Zechstein Group has been previously studied in the Norwegian sector of southern North Sea and salt structures and lithological heterogeneities have been observed and identified, studies in certain areas, such as the Søgne Basin, Sørvestlandet High, and Åsta Graben, are lacking and inadequate (Karlo et al., 2014; Jackson and Stewart, 2017; Mueller et al., 2019; Rowan et al., 2019; Marin et al., 2022). Furthermore, Norway intends to construct the Sørlige Nordsjø II wind farm near these structures, which has the potential to be a crucial component of future underground

energy storage facilities (Figure 3). There is a possibility that energy produced from this wind farm can be used to compress and store air in the subsurface. Stored compressed air can be utilized when the energy demand is high. Hence, it is imperative to acquire a full understanding of the Zechstein Group around the Sørlige Nordsjø II wind farm. Moreover, prior studies did not extensively focus on underground energy storage solutions in salt caverns in the Norwegian sector of the southern North Sea, and it is urgent to fill the gap of knowledge.
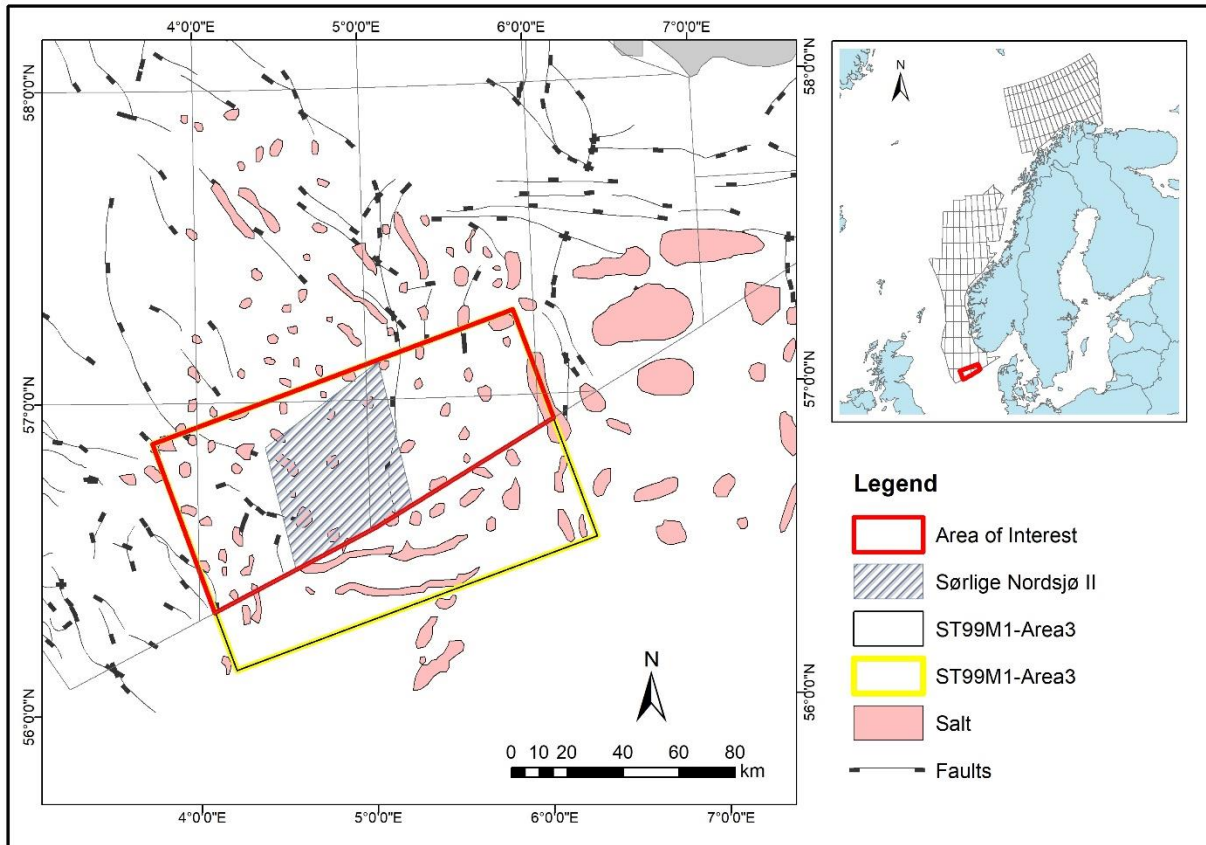
Figure 3: Location map of the study area, modified from Veibæk & Britze (1984) and NPD (2023).

To store energy in underground salt caverns, specific geological criteria must be met, including but not limited to an appropriate depth, thickness, the availability and efficiency of non-salt interbed, thickness of both salt and non-salt roof rocks, and the height-to-diameter ratio of the salt cavern (Duhan, 2018; Parkes et al., 2018). In the southern North Sea, important aspects such as the characterization of heterogeneities, depth, geometry, and thickness of salt formations were only briefly mentioned (Stewart, 2007; Karlo et al., 2014; Jackson and Hudec, 2017; Jackson and Stewart, 2017). Thus, it is crucial to study these salt formations and compositional variations of

the Zechstein Group to acquire knowledge about the geological requirements and challenges involved in using salt caverns for underground energy storage, particularly for CAES operations. Therefore, this study has defined an area of 6675 km^2 in the Norwegian sector of the southern North Sea for a pilot study (Figure 3). The goal of this study is to gain a better understanding of the salt formations in the Zechstein Group, with the aim of minimizing geological risks in CAES projects that involve salt caverns around the world. To achieve the goal, the following tasks will be carried out: (1) different types of salt structures will be evaluated by using seismic data; (2) the top and bottom of the Zechstein Group will be mapped and the bulk thickness of salt formations will be calculated; (3) internal compositions of the Zechstein Group will be examined and interpreted; (4) the 3D models of the salt formations will be generated; and (5) volumetric calculations will be performed to construct salt caverns on proposed reservoir area.

2. Salt Cavern Storage Types and Current Status

Different types of energy can be stored in salt caverns, including natural gas, hydrogen, and compressed air (Ozarslan, 2012). Among these, compressed air and hydrogen gas storage methods are the most promising candidates for large-scale energy storage applications and they are key resources for energy transition (Ibrahim et al., 2008).

2.1. Underground Hydrogen Storage (UHS) Applications

Hydrogen is a promising energy source that emits no harmful substances into the environment and has a high efficiency in converting energy. It is a fuel with a high heat value, complete combustion, and no pollutant emissions into the air (Ball and Weeda, 2015; Bunger et al., 2016; Tarkowski and Lankof, 2020; Yartys and Lototsky, 2004).

Underground hydrogen storage (UHS) in salt caverns has a long history. Up to date, hydrogen has been stored in three salt caverns, with one at Teesside, UK, since 1972 and two at the Gulf Coast in Texas, USA, since 1983 (Evans et al., 2009; Panfilov, 2016; Stone et al., 2009; Tarkowski, 2019). Storage of hydrogen in these caverns has been proven to be successful and safe over a long period of time (Evans et al., 2009; Panfilov, 2016; Stone et al., 2009; Tarkowski, 2019). In the UK, a British company stores 1 million cubic meters of 95% hydrogen and 3-4% CO_2 in three salt caverns at a depth of around 400 m with a pressure of 50 bar (Tarkowski, 2019). Stored hydrogen is consumed by nearby industrial plants for the production of ammonia and methanol. In Texas,

ConocoPhillips stores hydrogen with 95% purity in the Clemmons salt dome, with a cavern roof situated at a depth of approximately 850 m (Tarkowski, 2019). The cavern is cylindrical in shape, with a diameter of 49 m and a height of 300 m, and has a usable hydrogen capacity of 30 million cubic meters or 2520 metric tons (Tarkowski, 2019). The storage facility is directly connected to the Old Ocean Refinery (Tarkowski, 2019).

Compared to petroleum, hydrogen is the cleanest fuel and has a heating value of three times greater (Zhou, 2004). However, hydrogen also has several disadvantages that can be a source of problems during its storage in salt caverns. The hydrogen particles, due to their small size, are able to penetrate porous materials; at high temperatures, hydrogen diffuses in steel, causing corrosion and hydrogen embrittlement (Melaina et al., 2013; Tarkowski and Lankof, 2020). Low dynamic viscosity and molecular diameter of hydrogen cause its high mobility, which increases the risk of leakage from underground storage (Feldmann et al., 2016; Tarkowski and Lankof, 2020). Moreover, hydrogen is rarely a natural source, but a man-made fuel. Therefore, hydrogen bears a manufacturing cost, which made it cost three times higher than petroleum products (Zhou, 2004). In addition, the most frequently used hydrogen storage solutions in the industry, compression and liquefaction, are highly energy-consuming. Therefore, efficient and safe large-scale hydrogen storage is still challenging (Malachowska et al., 2022).

2.2. Compressed Air Energy Storage (CAES) Applications

Compared to the UHS, compressed air energy storage (CAES) is a storage technology capable of storing grid-scale (> 50 MW) electricity with the lowest cost and the lowest construction risk (Duhan, 2018). Most importantly, the CAES systems have several further advantages including having a relatively shorter starting time, being easily optimized to fit any specific site, providing a great economic benefit, and having large storage capacities (Salkuti and Jung, 2018). Currently, there are three commercialized CAES plants around the world, which utilize storage facilities hosted in salt caverns. The first of these plants is the Huntorf plant located in Germany, constructed in 1978. It stores 310,000 m^3 of compressed air in two caverns situated at a depth of 650 m with a deliverable power capacity of 290 MW (Crotogino et al., 2001; Jafarizadeh et al., 2020) (Figure 4). The second plant, the McIntosh plant in Alabama, was built in 1991 and stores compressed air in a large salt cavern with a total volume of 570,000 m^3 located at a depth of 460 m with a deliverable power capacity of 110 MW (Matos et al., 2022). The third and most recent plant, located in Goderich, Canada, was commissioned in November 2019 and has a small salt-cavern-

hosted storage facility with an installed deliverable power capacity of 1.75 MW (Borri et al., 2022; Gasanzade et al., 2023).
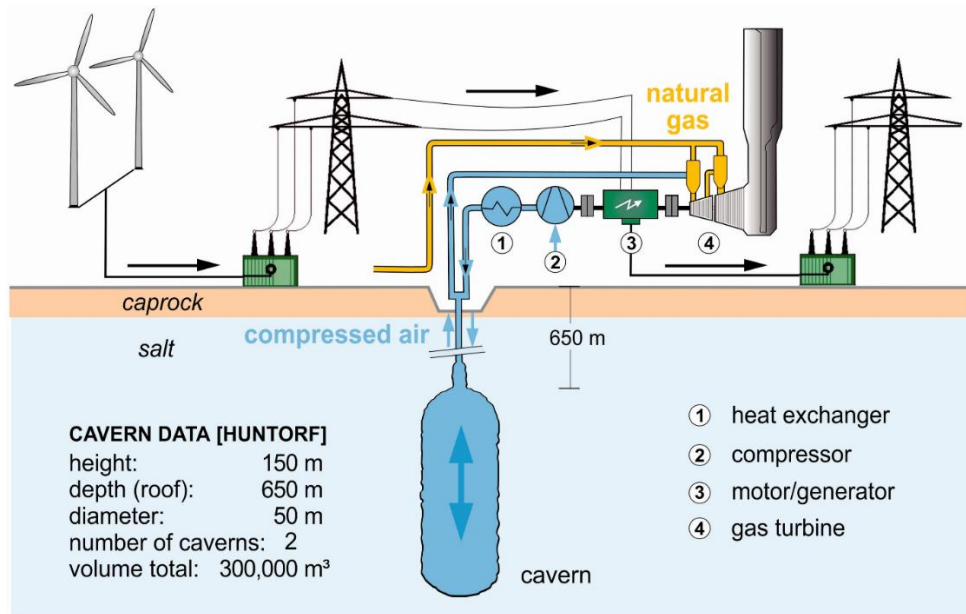
Figure 4: The principle of the Huntorf CAES power plant in Germany (Donadei and Schneider, 2022).

Several studies have examined the geological requirements for underground hydrogen storage operations (Table 1). The thickness of the bedded salt formations should be no less than 200m, while the salt formation's minimum and maximum depths should be 500 and 1400m, respectively. The height-to-diameter ratio should at least be 0.5. The presence of easily dissolvable K-Mg salts is also unwanted, as it could lead to gas leakage (Caglayan et al., 2020; Lankof et al., 2022; Lankof & Tarkowski, 2020; Tarkowski, 2019; Malachowska et al., 2022).

Table 1: Geological requirements for CAES operations. After Duhan (2018).

	Depth	Thickness	Interbed Thickness	Salt Cap Rock Thickness	Non-Salt Cap Rock Thickness	Height/Diameter Ratio	Cavern Spacing
Suitable	>250m and <1500m	> 20m	< 3m	> 0.25 * Diameter	> 0.33 * Diameter	> 0.5 * Diameter	> 3 * Diameter
Unsuitable	<250m and >1500m	< 20m	> 3m	< 0.25 * Diameter	< 0.33 * Diameter	< 0.5 * Diameter	< 3 * Diameter

2.3.   Geological Requirements to Be An Underground Storage Reservoir

Choosing a location for underground storage both for the CAES and UHS in salt deposits requires careful consideration of various crucial factors including the shape and depth of the site, the thickness of salt beds, the composition of reservoir rocks, and the solubility of the rocks (Tarkowski, 2019). Previous research by Parkes (2018) and Duhan (2018) identified a set of geological criteria that should be taken into account when considering underground storage in salt

caverns for CAES operations as shown in Figure 5 and Table 1. Below is the summary of key factors proposed by Duhan (2018):

Buried depth

To maintain the required pressure range of 4 to 8 MPa, suitable salt caverns for CAES are typically located at depths ranging from 250 m to 1500 m. Caverns shallower than 250 m may not be able to withstand pressures up to 8 MPa, leading to fracturing and limiting the operating pressure range. Conversely, caverns deeper than 1500 m are considered unsuitable, as the minimum pressure of 4 MPa may cause significant strain rates and excessive cavern closure during operation. In caverns, deeper than 1500 m, higher compression pressures are required, which need more energy consumption, or even results in notable energy loss. Parkes et al. (2018) also supported these depth criteria for salt cavern suitability in CAES operations.

Thickness of the salt structures

Salt cavern must be thick enough to support large volumes and ensure cavern stability. A thickness of at least 160 m is ideal for CAES operations. If the thickness is less than 20 m, the salt cavern is not suitable for the CAES. In bedded salt deposits, there may be non-salt interbeds that should be considered when selecting an underground salt cavern for the CAES operations. The thickness of these interbeds is critical, since if they are too thin, they may detach during the CAES operations, while if they are too thick, they may reduce the salt volume and divide the salt cavern. Hamilton (1971) suggests that the thickness of non-salt interbeds should not exceed 3 m.

Cap rock

Cavern stability is a critical consideration for CAES operations, and cap rock plays a significant role. The cap rock should be sufficiently thick to withstand the load and minimize cavern deformation while also serving as a barrier for trapped air. There are two types of cap rock, namely salt and non-salt. For salt cap rock, a thickness greater than 0.25 times the diameter of the salt cavern is recommended, whereas for non-salt cap rock, the thickness should be greater than 0.33

times the diameter of the salt cavern. The salt cavern's stability also depends on the height-to-diameter ratio. The cavern's height should be greater than 0.5 times its diameter to ensure stability.

Spacing of multiple caverns

In case there are plans to construct multiple caverns, the spacing between them should be greater than 3 times the diameter of the first cavern to secure the stability of the caverns.
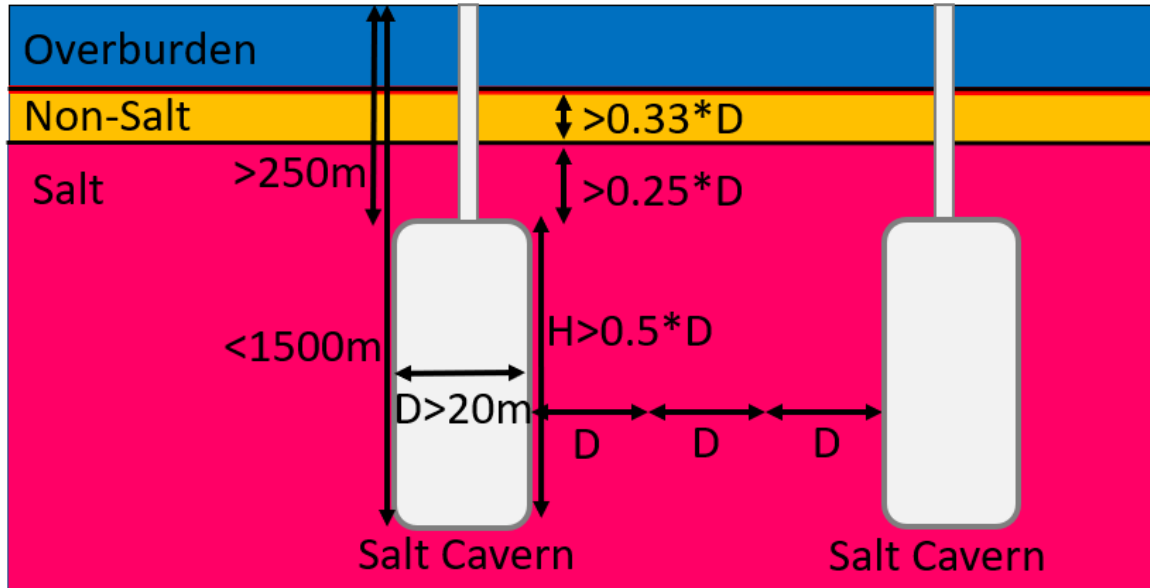
Figure 5: Geological requirements to be a CAES reservoir. After Duhan (2018).

The geological prerequisites for UHS operations are akin to those for CAES operations. Therefore, salt formations proposed for CAES operations can also be utilized for UHS operations.

3. Geological Setting
3.1. Tectonic Setting

The North Sea region has undergone an intricate geological transformation from the Cambrian era to the present, wherein it has been involved in various tectonic regions and sedimentary basins. In terms of the progression of basin formation, the evolution of the North Sea area can be categorized into the following subsequent stages: (1) Caledonian geosynclinal stage (Cambrian-Silurian), (2) Variscan geosynclinal stage (Devonian-Carboniferous), (3) Permo-Triassic intracratonic stage, (4) Taphrogenic rifting stage (Jurassic-Cretaceous), (5) Post-rifting intracratonic stage (Tertiary) (Ziegler and Hoorn, 1989).

A significant portion of the North Sea region's underlying crystalline basement underwent consolidation during the Caledonian orogenic cycle, while the eastern sectors of the North Sea encompass a late Precambrian basement complex (Ziegler and Hoorn, 1989). The Scottish-Norwegian Caledonides, extending across the northern part of the North Sea, exhibit a structural grain that trends in the northeast-to-southwest direction (Ziegler and Hoorn, 1989) (Figure 6). In contrast, the North German-Polish Caledonian fold belt, branching off from the Scottish-Norwegian Caledonides in the central North Sea, likely demonstrates a structural grain that trends from north to south in the central region, and from southeasterly to easterly in the south-central and southern parts of the North Sea (Ziegler and Hoorn, 1989).
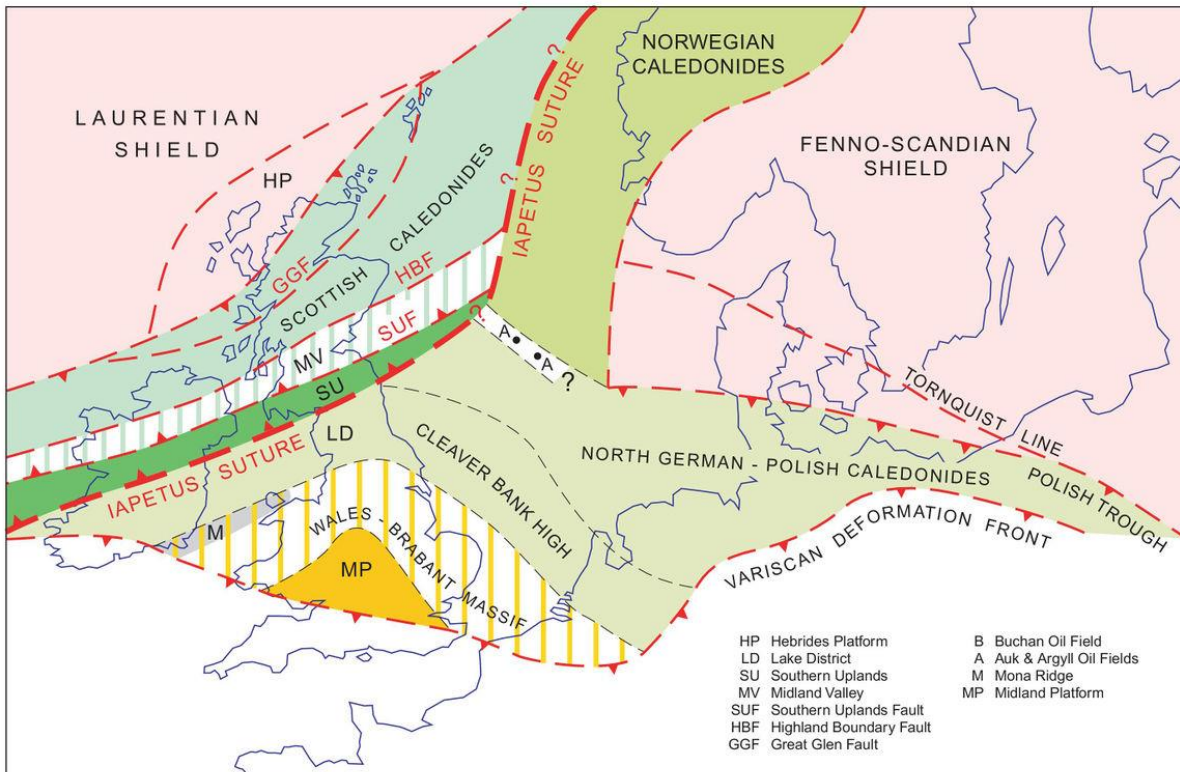
Figure 6: A regional tectonic map showing the Scottish-Norwegian Caledonides and the North German-Polish Caledonian fold belt (Glennie, K. W., et al., 2005).

During the Devonian and early Carboniferous periods, the southern region of the North Sea became a component of the Rhenohercynian basin, which emerged in the Mid-European and North German-Polish Caledonides area as a result of tensional forces (Ziegler and Hoorn, 1989). However, with the onset of the Variscan orogenic cycle in the late Visean period, the tensional environment of this basin came to an end, giving way to the development of the Variscan foreland

basin (Ziegler and Hoorn, 1989). In the late Carboniferous period, the central and southern areas of the North Sea were occupied by the more distant portions of this basin, where a wedge of paralic coal measures progressively expanded in a southward direction (Ziegler and Hoorn, 1989).

Salt tectonics started shortly after deposition with some examples of Permian-age salt structures (Stewart, 2007). The Zechstein Group, evaporite-dominated sediments, was deposited during a major transgression on the Late Permian after a thick succession of non-marine sediments (the Rotliegend Group) during the Early Permian (Lewis et al.,2013; Sørensen et al., 1992) (Figure 7). Salt sedimentary rocks found in the Norwegian sector of the North Sea are part of the Zechstein Group (Ziegler and van Hoorn, 1989). This deposition occurred in a trough that extended in an east-west direction and is known as the North Permian Basin (Ziegler and van Hoorn, 1989). The rim of the basin had carbonate banks, while the central trough had thick evaporites (Karlo et al., 2014). In the Early Triassic, the basin experienced faulting due to north-south rifting, which affected the Norwegian-Danish Basin (Karlo et al., 2014). Hanging-wall subsidence and increased sediment input resulted in the flow of the Zechstein Group and the development of thickened salt formations (Lewis et al., 2013). As a result, salt tectonism caused variations in thickness due to minibasin formation. In the Middle and Late Jurassic, a second phase of rifting occurred, further affecting the basin. The rifting continued into the Early Cretaceous period (Karlo et al., 2014). During the Middle Jurassic-to-Early Cretaceous, rifting caused the reactivation of salt tectonics, minor salt flow, and diapir rise occurred in previously thickened salt formations (Lewis et al.,2013; Sørensen et al., 1992). Since Late Cretaceous, the southern North Sea has experienced sporadic shortening, which caused some of the larger salt structures to be squeezed (Lewis et al.,2013; Sørensen et al., 1992).
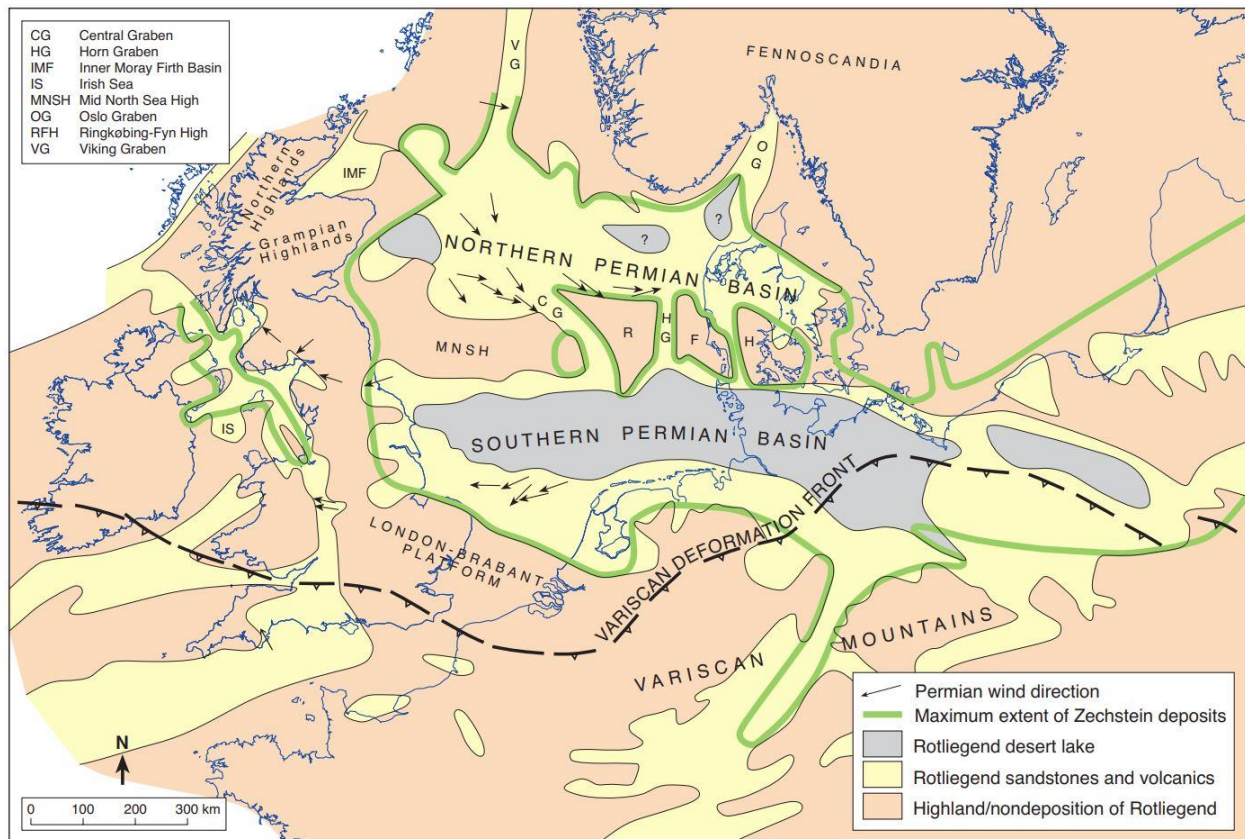
Figure 7: Sketch map of Permian sedimentary basins in the North Sea (The Geological Society of London, 2003).

3.2. Stratigraphy of the Zechstein Group

During the Late Permian, the Zechstein salt basin was formed due to a combination of factors including a rise in sea level and active rifting in the North Sea, which allowed a seaway to form between the Permian Basin and the Arctic Ocean (Pichat, 2022; Sørensen et al., 1992; Ziegler and van Hoorn, 1989). The development of the Zechstein group and the thick accumulation of evaporites occurred due to marine influxes in the Central European Basin, which provided the necessary brines and arid conditions (Pichat, 2022). The formation of the Zechstein evaporites was affected by changes in sea levels, which caused the formation to be divided into five cycles known as Z1 to Z5 (Duffy et al., 2023; Marin et al., 2023; Pichat, 2022) (Figure 8). These cycles have been recognized for the Zechstein Group in North Europe such as the Netherlands, Germany, and Poland. Although these cycles have not been officially recognized in the Norwegian sector of the North Sea, they share many similarities with other regions in North Europe (Marin et al., 2023). The evaporites in the Zechstein contain layers of shale, carbonate, sulfate, halite, and K-Mg salts arranged in sequences that were primarily influenced by the amount of seawater flowing into the

13

basin, and these inflows were linked to third or fourth-order sequences of eustatic variations (Duffy et al., 2023; Marin et al., 2023; Pichat, 2022). The first cycle of Zechstein evaporites, Z1 (Werra Fm), consists of coppery shale, carbonate, anhydrite, and salt, sometimes accompanied by layered claystone, limestone, and dolomite. Additionally, there are occurrences of K-Mg salts in the Z1. The Z1 cycle ends with a flat layer of upper anhydrite that was formed in water that was shallow or partially exposed to air. This upper anhydrite marks the beginning of the marine transgression of the subsequent Z2 evaporite cycle (Pichat, 2022). The Z2 (Stassfurt Fm) consists of carbonate, basal anhydrite, salt, and roof anhydrite. In the main basin, over 600 meters of halite intermixed with K-Mg salts accumulated, filling the depression beyond the former carbonate-anhydrite platform, where salt deposits remained relatively thin, only 10 to 100 meters thick. During the final stages of halite infill, the basin was flattened and sylvite and carnallite salts developed regionally at the top of the Z2 salt. The second cycle Z2 contains a significant amount of halite and has been mostly utilized for salt cavern construction in areas such as Germany, Poland, or the Netherlands. The Z2 ends with an anhydrite layer (Z2 Roof Anhydrite), indicating the gradual influx of seawater (Marin et al., 2023; Pichat, 2022). The Z3 (Leine Fm) consists of gray salt clay, carbonate, main anhydrite, and Z3 salt, with the latter estimated to be as thick as 400 m. The Z3 salt consists of a basal layer of halite and an upper layer of K-Mg salts like kieserite, carnallite, and sylvite (Pichat, 2022). In contrast, the Z4 (Aller Fm) is composed of red salt clay, pegmatite anhydrite, and Z4 salt. Its middle part has K-Mg salt deposits, while the upper part is characterized by halite and claystone alternations (Pichat, 2022). The Z5 (Ohre Fm) is composed of a basal claystone layer several meters thick, followed by halite deposits that can be as thick as 15 m (Pichat, 2022). Finally, the Zechstein evaporites are unconformably overlaid by the Zechstein Upper Claystone Formation (ZEUC), which can be up to 50 m thick and composed of red and gray anhydrite claystones and sandstones deposited in a lacustrine to mudflat environment (Pichat, 2022).

Age	Group	Fm.		Lithology			Thickness	Units
			S	Shelf	Slope	Main Basin N	100 - 3500 m	Postsalt
Late Permian	Zechstein	ZEUC Z5	Aller Ohre		Zechstein Upper Claystones			
		Z4			Z4 salt	Z5 salt Pegmatite Anhydrite	< 10 - 50 m	Z4 salt
		Z3	Leine			Red Salt Clay Z3 Salt	50 - 300 m	Z3 salt
					Z3 Carbonate	Z3 Main Anhydrite	30-150 m	Z3 stringers
		Z2	Stassfurt		Z2 Roof Anhydrite	Grey Salt Clay Z2 Salt Basal Anhydrite	< 50 m - 1000 m	Z2 salt
		Z1	Werra		Z1 Salt Kupferschiefer	Z2 Carbonate Z1 Anhydrite Z1 Carbonate	100 - 300 m	
				Claystone ▮ Salt ▮ Limestone to dolostone ▮ Anhydrite ▮ Sandstone ▮				Presalt

Figure 8: General lithostratigraphic chart of the Zechstein in the Netherlands (Pichat, 2022).

4. Data and Methodology

In this study, subsurface data from the Norwegian Petroleum Directorate (NPD) Diskos database were employed, which comprised one 3D seismic cube, multiple 2D seismic lines, well logs, well reports, and core samples, and spanned an extensive area of 6675 km^2 (Figure 9). The 3D seismic survey, named ST99M1-AREA3, only captured a fraction of the study area, specifically the Southeast portion measuring 3070 km^2. Consequently, the remaining region was interpreted by using more than 140 km of 2D seismic lines. The seismic dominant frequencies ranged from 10 to 50 Hz, with varying quality from good to poor.
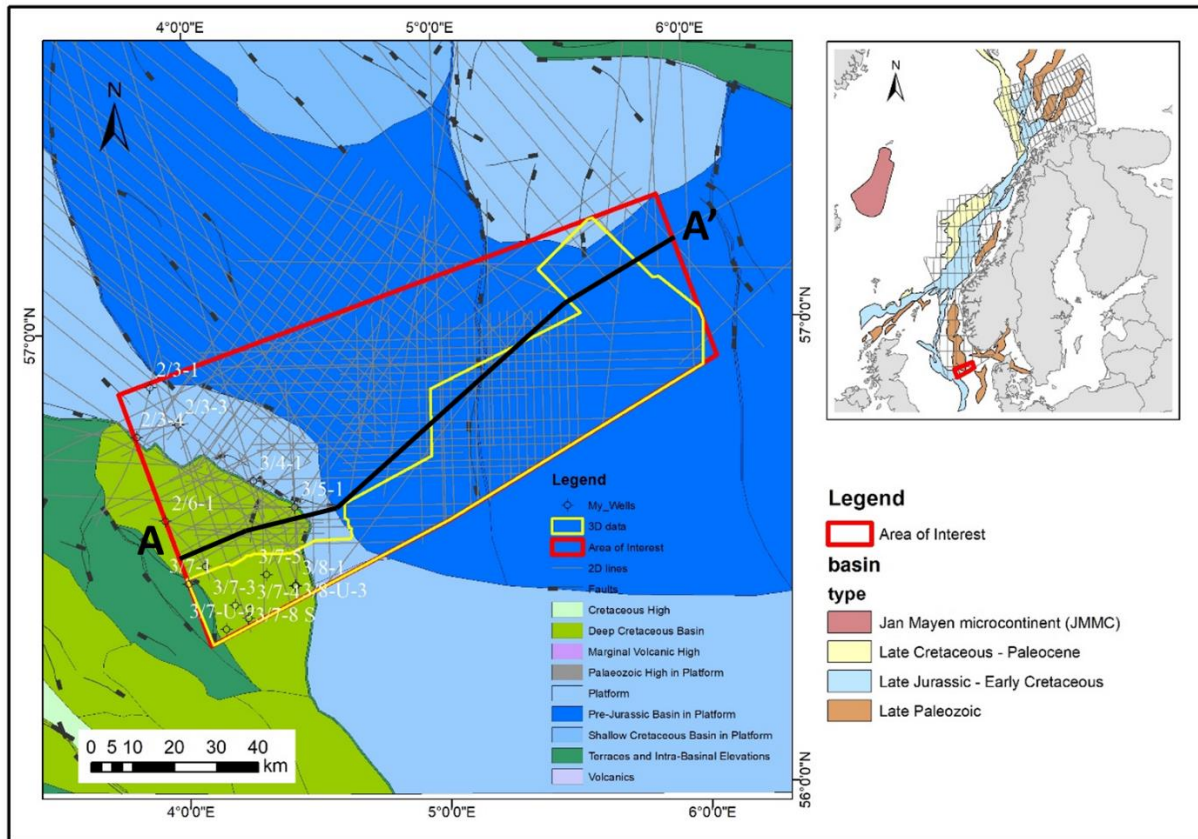
Figure 9: Available data in the study area.

The wells selected for this study were chosen based on their ability to penetrate either the whole or most of the Zechstein Group, or because they penetrated a salt diapir. The former was used to interpret the top and base of the Zechstein Group, and 14 wells in the western part of the study area were identified as suitable for this purpose. These include wells 2/3-1, 2/3-3, 2/3-4, 2/6-1, 3/4-1, 3/5-1, 3/7-1, 3/7-3, 3/7-4, 3/7-5, 3/7-8 S, 3/7-U-9, 3/8-1, and 3/8-U-3 (Figure 9). On the other hand, wells that penetrated salt diapirs were used to interpret the seismic internal facies of the salt diapirs in the region, to better understand their compositional variations. However, no such well was present in the study area, therefore, wells located near the study area were used instead as reference wells. These wells were analyzed using gamma-ray well logs, well reports, and core samples to determine the composition of the Zechstein Group. It is assumed that the composition of the Zechstein Group in the study area is similar to that in the reference wells. Table 2 lists the names and usages of the reference wells used in this study.

Wells	Data Type		
	Well Logs	Core Samples	Well Reports
1/6-5		X	X
3/7-2	X		X
7/3-1	X		X
8/3-1	X	X	X
11/9-1	X		X
15/5-3	X	X	X

Horizon interpretations have been conducted by tracking either the positive amplitudes (peaks) or the negative amplitudes (troughs) within the seismic data. The peaks are visualized in red, the troughs in blue, and the zero crossings are represented as narrow white bands (Figure 10).
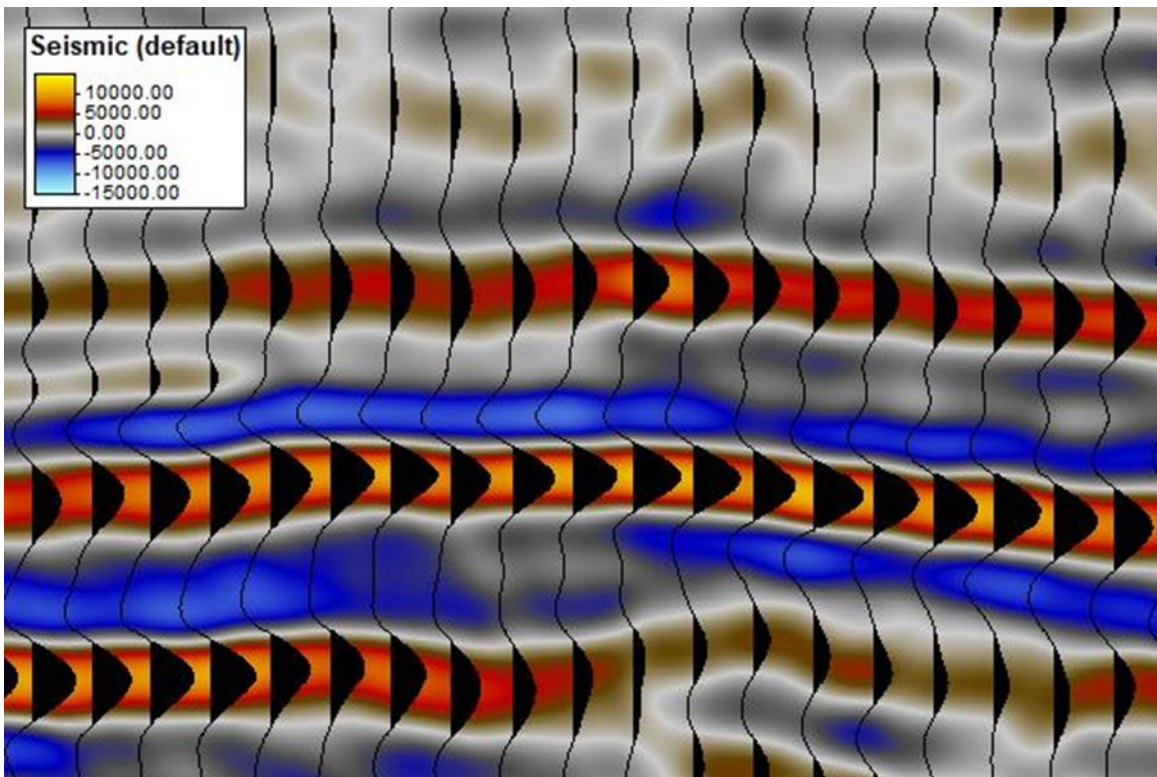
Figure 10: A close-up image of the seismic data showing peaks and troughs.

Accurate well ties play a crucial role in selecting the appropriate reflection to follow. When conducting interpretations without well ties, the continuity of the reflection and the stratigraphic image assume utmost importance in determining the reflection to be interpreted. Several reference

horizons, derived from well ties, were established and interpreted across both the 2D seismic lines and the 3D seismic cube (Figure 11). These horizons are detailed in Chapter 5. The main emphasis of this study revolved around the Zechstein Group, thereby encompassing the interpretation of its upper and lower boundaries. The interpretation of the Rotliegend Group, positioned at the base of the Zechstein Group, was relatively straightforward due to its distinct high-amplitude and uninterrupted seismic reflections (Figure 12). Nonetheless, the interpretation of the upper boundary of the Zechstein Group proved challenging due to the low amplitude contrasts, resulting in some uncertainty within the seismic interpretation. These horizon interpretations were utilized for generating surface maps and thickness maps.
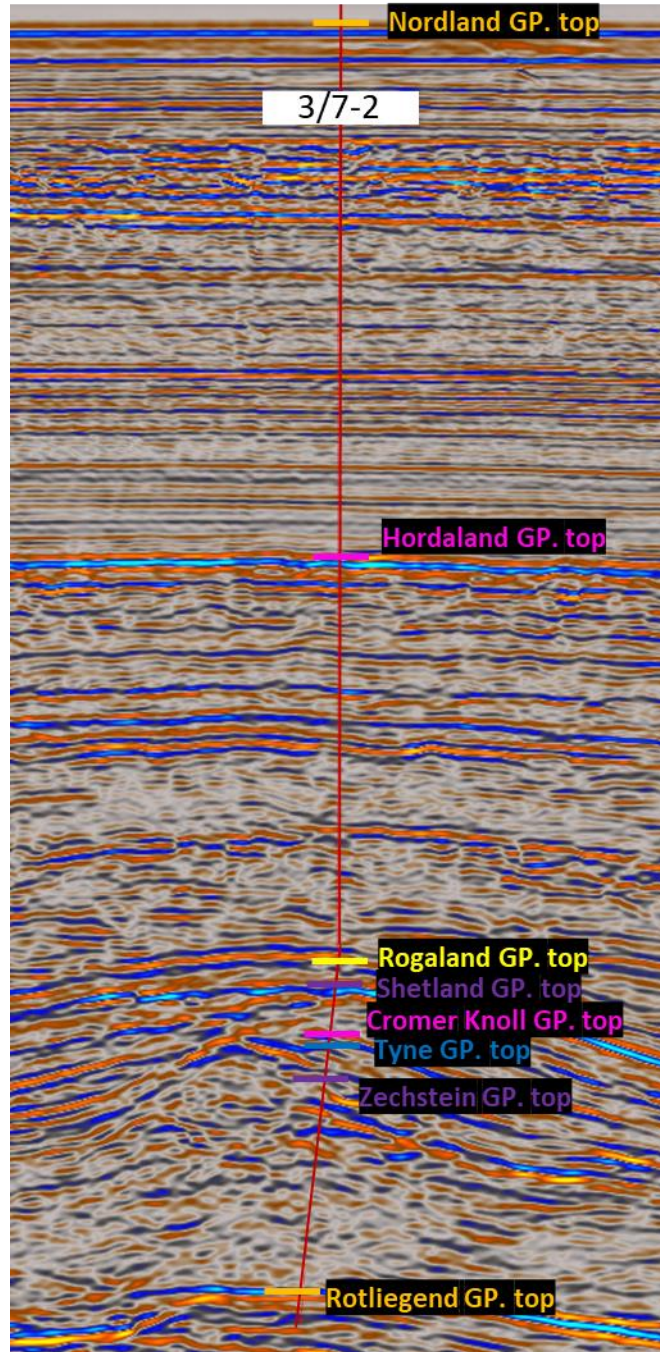
Figure 11: Well ties from well 3/7-2.

Landmark DecisionSpace was utilized for seismic interpretation to generate surface maps of the top and base Zechstein Group, as well as a thickness map of the Zechstein Group. Additionally, SLB Petrel was employed to visualize the 3D representations of the salt diapirs and their internal compositions. Furthermore, time-slice interpretation was conducted using SLB Petrel. Moreover,

the required maps were generated in ArcGIS and the figures were improved using Adobe Illustrator.

5. Observations and Interpretation
5.1. Regional Seismic Line

The study area comprises 8 distinct geological groups: Nordland, Hordaland, Rogaland, Shetland, Cromer Knoll, Tyne, Zechstein, and Rotliegend groups. A seismic line running from southwest to northeast across the study area illustrates the stratigraphic profile with and without interpretation (Figure 12). The horizon interpretations were meticulously correlated based on well tops.

The Rotliegend Group is composed of volcanic rocks at the bottom and sedimentary rocks, mostly sandstone, at the top (NPD, 2023). On the seismic profile, the horizon of the top Rotliegend Group displays continuous and parallel seismic reflectors with an abrupt amplitude change. It is displaced due to the presence of multiple normal faults. Wedge-shaped strata thickening towards fault planes are observed in some hanging-wall blocks of normal faults. The presence of wedge-shaped strata related to normal faults indicates evidence of syn-rift deposition (Osagiede et al., 2020). This is in line with previous studies on Permo-Triassic rifting (Fɪrseth et al., 1997).

The Tyne Group consists mostly of claystone, while the Cromer Knoll and Shetland Groups are mostly comprised of mudstones and siltstones, with the Cromer Knoll containing a significant amount of sandstone (NPD, 2023). The Rogaland Group is primarily sandstone, whereas the Hordaland and Nordland Groups are characterized by marine claystone (NPD, 2023).
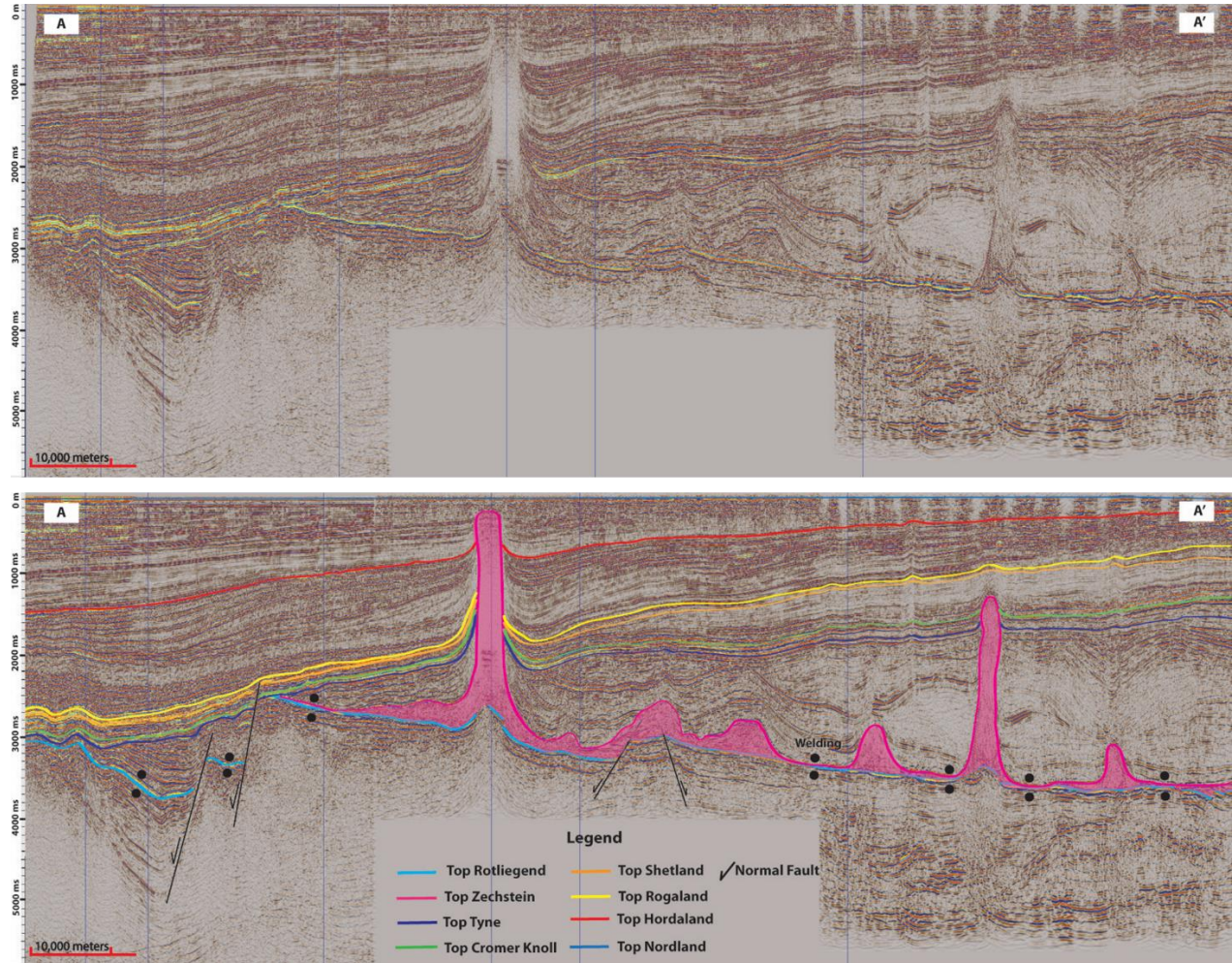
Figure 12: General Cross-Section of The Study Area.

5.2.   Seismic Expressions of Salt Structures

The Zechstein Group is the main focus of this study. The top of the Zechstein Group is treated as the top of the salt formation, whereas the top of the Rotliegend Group is treated as the bottom of the salt formation throughout the study area. Therefore, the seismic interpretation of salt formation was completed by interpreting horizons along the tops of the Rotliegend Group and the Zechstein Group. The other geological groups were only considered to calculate the depth of the salt formations and were not interpreted.

Upon completing the salt interpretation in the study area, five different types of salt structures are observed based on the degree of deformation. These types include bedded salt layers, salt pillows, salt rollers, salt diapirs, and salt walls (Figure 13).

21

Bedded salt layers

Bedded salt layers appear at a depth varying from 3000 to 4500 ms, with a TWT thickness varying from 30 to 150 ms. They are non-deformed structures in general and show gradual thickness changes laterally (Jackson and Talbot, 1986; Wu et al., 2015) (Figure 13a). The cleanest seismic image is typically obtained from bedded salt layers when compared to other types of salt structures. These bedded salt layers consist of numerous thin layers of seismic reflectors that are parallel, continuous, and of medium amplitude. Additionally, these layers are interspersed with discontinuous seismic reflectors of low amplitude.

Salt Pillows

Salt pillows appear at depths varying from 2200 to 2800 ms, with a TWT thickness varying from 200 to 800 ms. Salt pillows are formed when a layer of salt is compressed between two sedimentary rock layers, leading to a rounded and cylindrical shape. They are usually wider than their height and can vary in size from several meters to several kilometers in diameter, distinguishable by their shapes (Jackson and Talbot, 1986; Wu et al., 2015) (Figure 13b). During the examination of seismic images depicting salt pillows, it was noticed that the seismic reflectors, characterized by their parallel, continuous, and medium amplitude nature, undergo disturbance and adopt a dome-like configuration due to the deformation of the salt formation. Consequently, the seismic image appears to be more disordered, with discontinuous seismic reflectors of lower amplitude occupying greater volumes.

Salt Rollers

Salt rollers appear at depths varying from 2000 to 2800 ms, with a TWT thickness varying from 300 to 1000 ms. They are characterized by a rolling or cylindrical shape, often elongated, with a central axis comprised of salt. Salt rollers typically form due to the movement and deformation of salt layers or domes within the subsurface (Jackson and Talbot, 1986; Wu et al., 2015) (Figure 13c). Much like salt pillows, the seismic reflectors characterized by their parallel, continuous, and medium amplitude characteristics experience disruption as a result of salt formation deformation. As a consequence, the seismic image displays increased disorder, with larger volumes being occupied by discontinuous seismic reflectors of lower amplitude.

Salt diapirs

Salt diapirs appear at depths varying from 200 to 1500 ms, with a TWT thickness varying from 1500 to 3000 ms. They are dome-shaped geological formations formed when salt rises from its original location and penetrates the overlying rock layers, as shown in Figure 13d. Due to the unique properties of salt, such as its lower density compared to most rocks and its capacity to flow over long periods of time, the pressure and density variations between the salt and the surrounding rock can cause the salt to deform and rise upward, resulting in a dome-shaped structure (Jackson and Talbot, 1986; Schultz-Ela et al., 1993; Wu et al., 2015). Salt diapirs seem to exhibit the most turbulent seismic image as a consequence of significant deformation within the salt formation. This leads to a prevalence of discontinuous and structureless seismic reflectors with lower amplitudes, occupying larger volumes in comparison to other types of salt structures.

Salt Wall

Only one salt wall is observed in the study area, it appears at a depth of around 800 ms, with a thickness of 2200 ms and a length of around 17 km. A salt wall is a type of geological structure that results from the upward movement of a large body of salt through overlying sedimentary rock layers. As the salt rises, it can create a wall-like structure that can stretch for several kilometers and have a height of several hundred meters (Jackson and Talbot, 1986). It displayed the same properties as salt diapirs. As a result, it will not be distinguished separately in subsequent sections of this study.
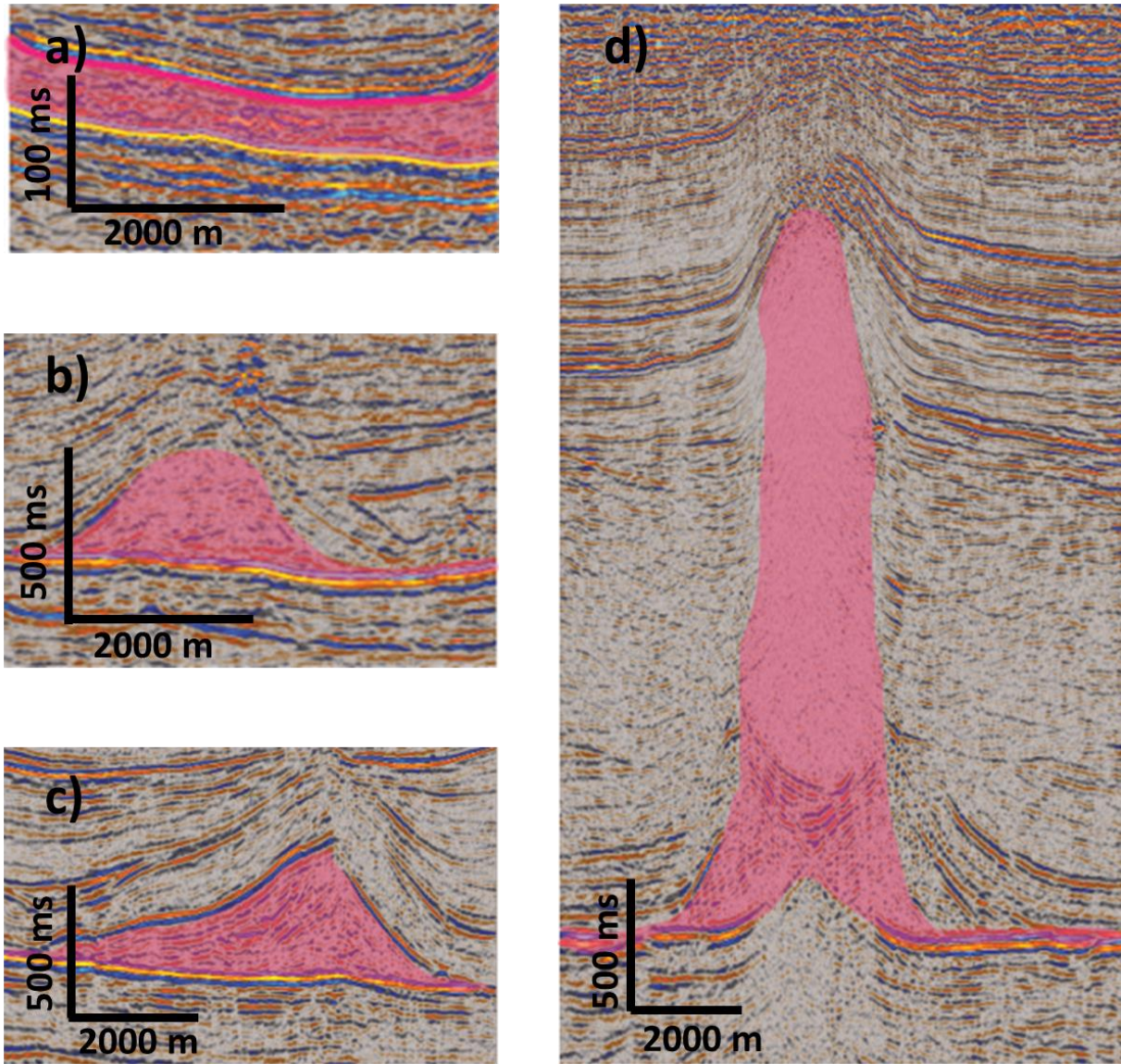
Figure 13: Different types of salt structures. (a) an example of a bedded salt layer in the study area; (b) an example of a salt pillow in the study area; (c) an example of a salt roller in the study area; (d) an example of a salt diapir in the study area.

Furthermore, significant anomalies with high amplitudes were identified in specific areas, for example surrounding the diapirs or beneath bedded salt layers. These anomalies indicate significant variations of acoustic impedance, which can be resulted from abrupt lithological changes or even the presence of hydrocarbon. If there exist hydrocarbon reservoirs, the salt formation itself can act as a seal rock for such resources. However, it is important to note that this study does not primarily focus on hydrocarbon exploration or prospect evaluation. Therefore, any recommendations regarding the possible presence of hydrocarbons will be discussed in the further work section.

5.3. Geological Mapping

Two-way travel time (TWT) Structural maps of the bottom of the Rotliegend Group and the top of the Zechstein Group were generated and presented in Figure 14. The grids of these two structural maps are filled with a color ramp, from red (shallow) to blue (deep).

Top Rotliegend Group structural map

The buried depth of the top Rotliegend Group varies from 2500 to 4500 ms in TWT. The study area is divided by two normal faults into three fault blocks. The normal fault in the southwest is 47 km long. It shows a curved shape with overall southwest dipping. The maximum fault throw along the top Rotliegend Group is 1200 ms. The other fault to the northeast is south-southwest striking and west-northwest dipping according to the Right Hand Rule. It is a plane fault and shows little curvature. The maximum fault throw along the top Rotliegend Group is 500 ms.

The southwestern and middle blocks show an overall northeast-dipping monocline, with buried depth varying from 3000 to 4500 ms and 2500 to 3600 ms, respectively. The southeastern block shows a syncline feature, with buried depth varying from 3000 to 3600 ms.

Top Zechstein Group structural map

The two normal faults from the top Rotliegend Group are mapped in the top Zechstein Group structural map. They inherited geometry from deep structures. For the curved normal fault to the southwest, the maximum throw along the top Zechstein Group is 1800 ms. By contrast, the fault throw for the other normal fault is reduced significantly, which is 600 ms at maximum.

The buried depth of the top Zechstein Group ranges from 500 to 4500 ms. The deepest part is located in the hanging-wall block of the curved normal fault. The shallow parts of the top Zechstein Group show a scattered distribution. The distribution of structural highs coincides with the location of either salt pillows, salt rollers, salt diapirs, or a salt wall. The shallowest part of the top Zechstein Group is related to a salt diapir.

Zechstein Group thickness map

A thickness map of the Zechstein Group was simply generated by using the top Zechstein Group structural map subtracting the top Rotliegend Group structural map (Figure 15a). The thickness of

the Zechstein Group ranges from 0 to 3000 ms. Zero thickness on the map indicates the localities of welded salt structures on seismic profiles (Figure 12).

Local areas with a thickness of 2500 ms, 2000 ms, 1500 ms, and 1000 ms were observed, which points to the different types of salt structures in the area. The analysis revealed that salt pillows constitute the majority of the study area, followed by a substantial number of salt diapirs. There is only one salt wall on the eastern side of the study area, and a few salt rollers exist in the study area. The remaining area is covered by very thin bedded salt layers. The distribution of different types of salt structures is highlighted in Figure 15b. The numbers of salt pillows, salt rollers, salt diapirs, and salt wall are 40, 4, 30, and 1, respectively.
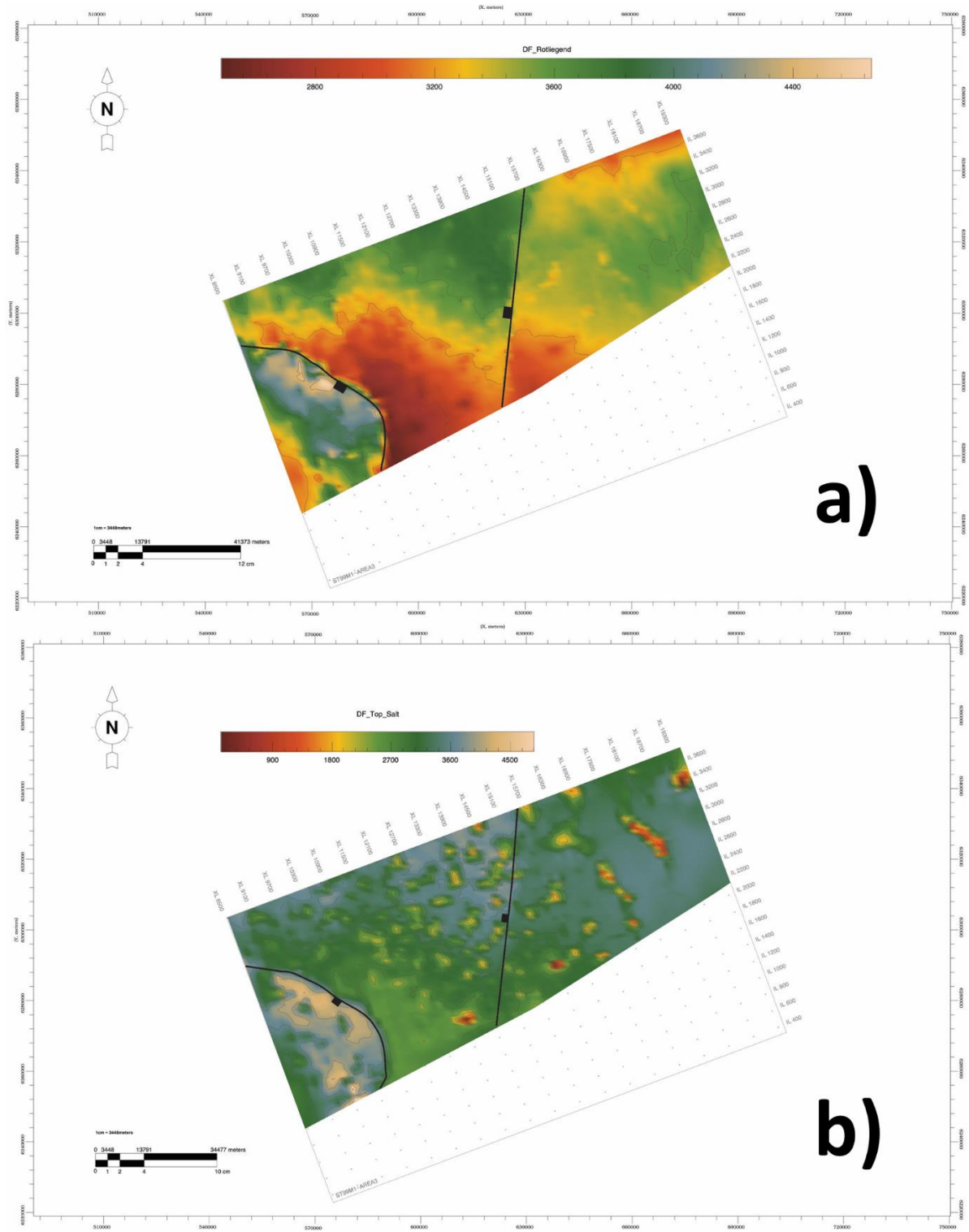
Figure 14: Structural maps. (a) structural map of the top Rotliegend Group; (b) structural map of the top Zechstein Group.
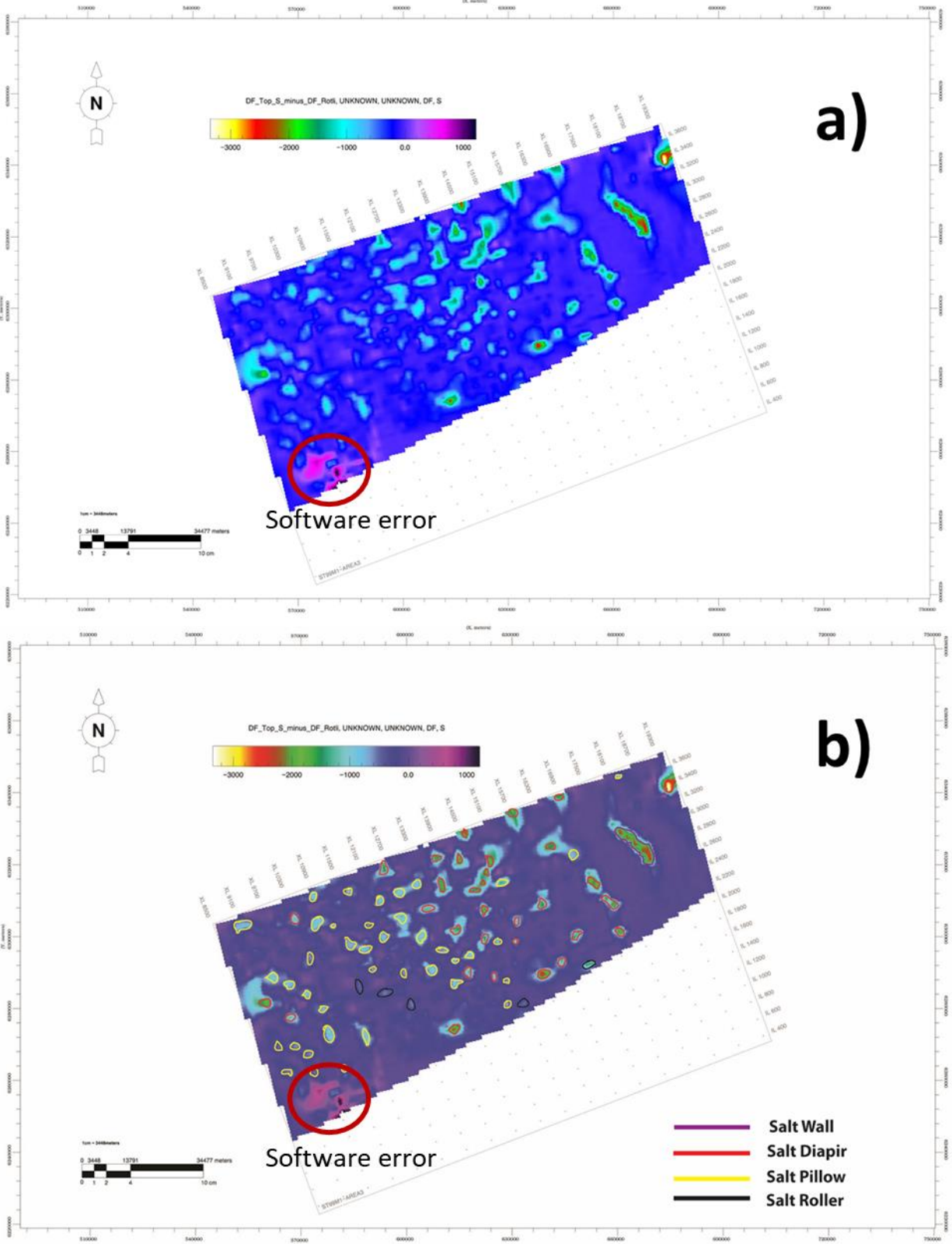
Figure 15: Thickness maps. (a) thickness map of the Zechstein Group; (b) localization of different types of salt structures on the map.

5.4. Internal Seismic Facies Classification

In order to determine the most suitable salt structures for compressed air energy storage reservoirs in the study area, various salt structures were compared and evaluated. Salt diapirs are especially focused as they induced the suitability of CAES operations in a buried depth of less than 150 m (Table 1; Figure 14b).

Seismic facies for internal structures of salt diapirs were analyzed to identify the best location to create salt caverns. Based on their seismic amplitude, dominant frequency, seismic structure, and seismic continuity, the diapirs were interpreted to have two main seismic facies; halite-dominated and anhydrite-dominated (Table 3). Five sub-facies are further classified, as I-1 and I-2 sub-facies in halite-dominated facies and as II-1, II-2, and II-3 in anhydrite-dominated facies.

Subsequently, since there was a lack of well data that penetrated the salt diapirs in the study area, the internal facies of targeted salt diapirs were defined by correlating nearby wells as reference, as they penetrated salt diapirs. Gamma-ray logs, well reports, and core samples of these reference wells were used to determine the classified internal facies.

5.4.1. Seismic Facies I: Halite-dominated salt structures

Within salt diapirs, seismic observations revealed volumes characterized by seismic reflectors of low amplitude, discontinuous nature, predominantly homogeneous, and lacking discernible structure. These observations led to the interpretation that these volumes correspond to salt structures predominantly composed of halite.

Seismic facies I-1

Based on seismic observations, seismic facies I-1 exhibits seismic reflectors that are characterized by discontinuous and structureless patterns with low amplitude, and a medium frequency of 25 Hz. The gamma-ray log response of the corresponding seismic pattern observed in the reference well 7/3-1 displays an even block with a sharp top and base, accompanied by a low gamma-ray (GR) value of around 30 API. Additionally, the core sample obtained from the reference well 15/5-3, which displays comparable seismic and gamma-ray log responses, has been identified as halite (Marin et al., 2023). Consequently, seismic facies I-1 is likewise interpreted as homogeneous halite.

Seismic facies I-2

Based on seismic observations, seismic facies I-2 exhibits seismic reflectors that are characterized by discontinuous and structureless patterns with low amplitude with low to medium intercalations, and a medium frequency of 25 Hz. The gamma-ray log response of the corresponding seismic pattern observed in the reference well 15/5-3 displays a saw teeth shape, accompanied by a low gamma-ray (GR) value of around 50 API. Additionally, the core sample obtained from the reference well 15/5-3, which displays comparable seismic and gamma-ray log responses, has been identified as halite, occasionally intercalated with very thin claystone or sylvinite layers (Marin et al., 2023). Consequently, seismic facies I-2 is likewise interpreted as halite, occasionally intercalated with very thin claystone or sylvinite layers.

5.4.2.   Seismic Facies II: Anhydrite-dominated salt structures

Seismic observations within salt diapirs identified volumes displaying seismic reflectors characterized by medium to high amplitude, continuous, and parallel patterns. These observations led to the interpretation that these volumes correspond to salt structures predominantly composed of anhydrite.

Seismic facies II-1

Based on seismic observations, seismic facies II-1 exhibits seismic reflectors that are characterized by continuous and parallel patterns with medium amplitude, and a medium frequency of 35 Hz. The gamma-ray log response of the corresponding seismic pattern observed in the reference well 3/7-2 displays an even block with a sharp top and base, accompanied by a high gamma-ray (GR) value ranging from 160 to 180 API. Additionally, the core sample obtained from the reference well 1/6-5, which displays comparable seismic and gamma-ray log responses, has been identified as anhydrite with shale intercalations (Marin et al., 2023). Consequently, seismic facies II-1 is likewise interpreted as anhydrite with shale intercalations.

Seismic facies II-2

Based on seismic observations, seismic facies II-2 exhibits seismic reflectors that are characterized by continuous and parallel patterns with low to medium amplitude, and a medium frequency of 30 Hz. The gamma-ray log response of the corresponding seismic pattern observed in the reference well 8/3-1 displays an hourglass shape, accompanied by a high gamma-ray (GR) value ranging
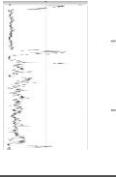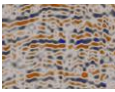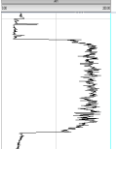
from 150 to 220 API. Additionally, the core sample obtained from the reference well 8/3-1, which displays comparable seismic and gamma-ray log responses, has been identified as anhydrite with intercalations of shale and siltstone intercalations (Marin et al., 2023). Consequently, seismic facies II-2 is likewise interpreted as anhydrite with shale and siltstone intercalations.

Seismic facies II-3

Based on seismic observations, seismic facies II-3 exhibits seismic reflectors that are characterized by continuous and parallel patterns with medium to high amplitude, and a medium frequency of 35 Hz. The gamma-ray log response of the corresponding seismic pattern observed in the reference well 11/9-1 displays an even block with a sharp top and base, accompanied by a high gamma-ray (GR) value ranging from 160 to 180 API. Additionally, the core sample obtained from the reference well 1/6-5, which displays comparable seismic and gamma-ray log responses, has been identified as anhydrite with intercalations of shale and dolomite intercalations (Marin et al., 2023). Consequently, seismic facies II-3 is likewise interpreted as anhydrite with shale and siltstone intercalations.

Table 3: Seismic internal facies of the salt diapirs.

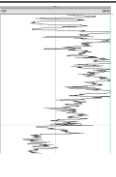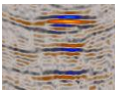| Seismic Facies		Description						Definition
Class	Subclass	Seismic Image		Reference Well	Gamma-Ray Log (0 - 200 API)		Core Sample	
I Halite Dominated	I-1		Low amplitude, medium frequency (25 Hz), discontinuous, structureless	7/3-1 & 15/5-3		Even block with sharp top & base, 1000+ m thickness, low GR value (around 30 API)	A sample of pure Halite from well 15/5-3 (Marin et al., 2023)	Halite
	I-2		Low amplitude with medium to low intercalations, medium frequency (25 Hz), discontinuous, structureless	15/5-3		Saw teeth, hundreds of meters thickness, low GR value (around 50 API)	A sample of Halite with a thin intercalation with Sylvite and Claystone from well 15/5-3 (Marin et al., 2023)	Halite, occasionally intercalated with very thin Claystone or Sylvinite layers
II Anhydrite Dominated	II-1		Medium amplitude, medium frequency (35 Hz), continuous, parallel reflectors	3/7-2 & 1/6-5		Even block with sharp top & base, 100+ meters thickness, high GR value (160-180 API)	A sample of Anhydrite embedded with a competent lithology from well 1/6-5 (Marin et al., 2023)	Anhydrite with Shale intercalation
	II-2		Medium to low amplitude, medium frequency (30 Hz), continuous, parallel reflectors	8/3-1		Hour glass, tens of meters thickness, high GR value (150-220 API)	A sample of Anhydrite intercalated with Siltstone from well 8/3-1 (Marin et al., 2023)	Anhydrite with Shale and Siltstone intercalation
	II-3		Medium to high amplitude, medium frequency (35 Hz), continuous, parallel reflectors	11/9-1 & 1/6-5		Even block with sharp top & base, tens of meters thickness, high GR value (160-180 API)		Anhydrite with Shale & Dolomite intercalation

Two salt diapirs in the southern part of the study area, named "Diamond diapir" and "Ellipsoid Diapir" based on their shapes, were selected to display the distribution of the above seismic facies along inline and crossline directions.

The Diamond diapir is about 2 km in size (Figure 16). The top of the diapir is buried at a depth of 200 ms in TWT. Halite-dominated facies I is observed in the middle of anhydrite-dominated facies II, with sub-facies II-1 and II-2 on the top and II-3 in the bottom. Buried depth of facies I ranges from 1000 ms to 2000 ms. Most importantly, sub-facies I-1 is buried in the depth from 1200 ms to 1800 ms.
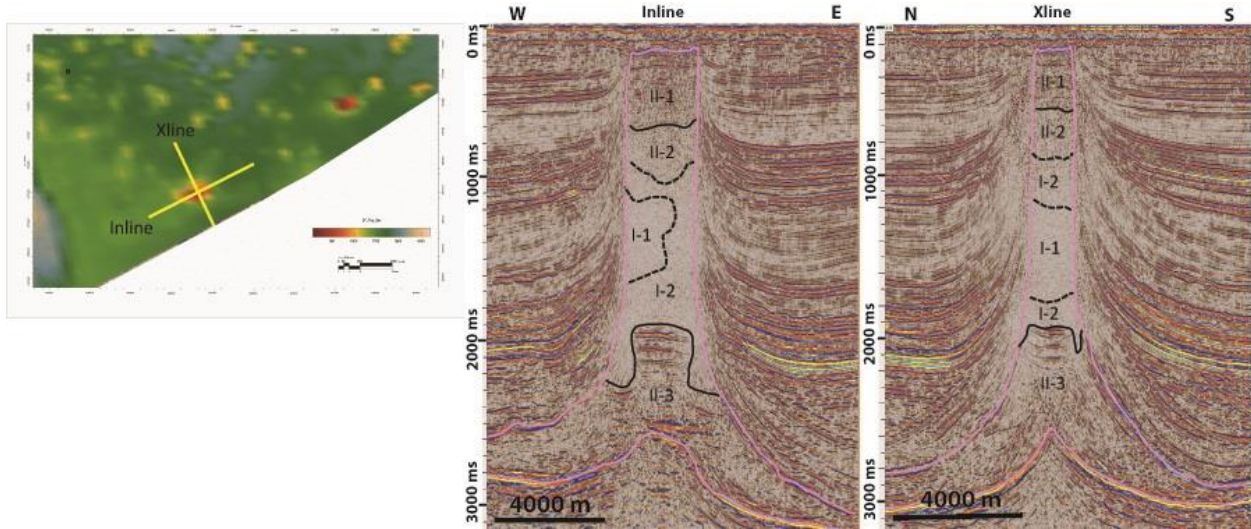
Figure 16: Seismic internal facies of the Diamond diapir.

The Ellipsoid diapir is about 1.5 km in size (Figure 17). The top of the diapir is buried at a depth of 200 ms in TWT. Similar to the Diamond diapir, halite-dominated facies I is observed in the middle of anhydrite-dominated facies II, with sub-facies II-1 and II-2 on the top and III-3 in the bottom. Buried depth of facies I ranges from 800 ms to 2200 ms. Most importantly, sub-facies I-1 is buried in the depth from 1100 ms to 2000 ms.
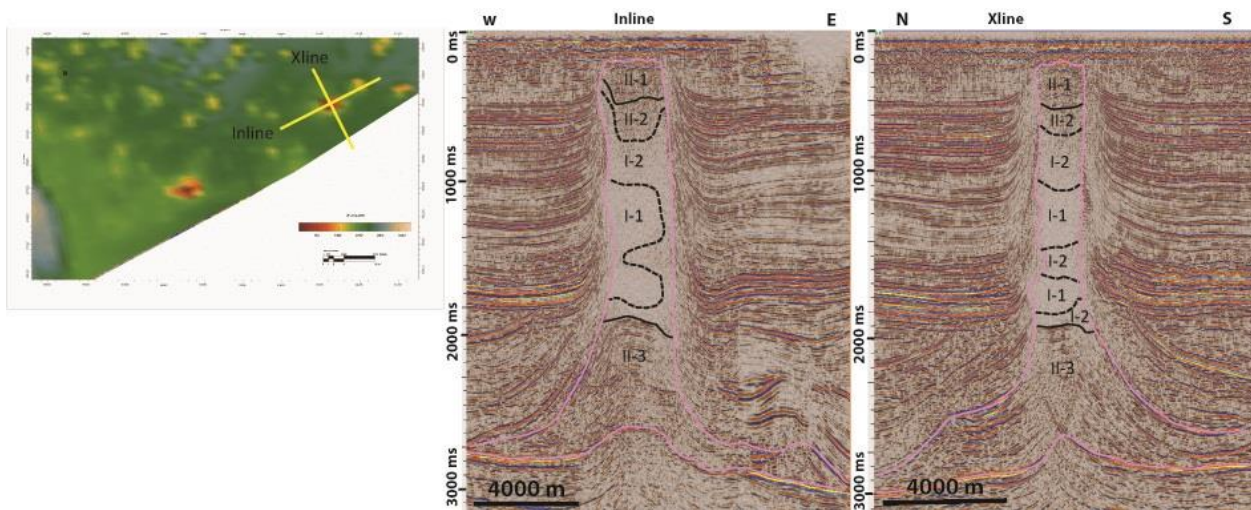
Figure 17: Seismic internal facies of the Ellipsoid diapir.

5.5. Seismic facies on time slices

In order to provide a comprehensive 3D interpretation of the internal seismic facies, a time-slices interpretation was conducted in addition to the inline and crossline interpretations. This interpretation was performed at certain depths based on the expected significant changes in the

internal composition of the selected diapirs. The results of the time-slices interpretation supported the inline and crossline interpretations.

For the Diamond diapir, TWT slices were generated in 400 ms, 700 ms, 1550 ms, 1850 ms, and 1960 ms (Figure 18). At a depth of 400 ms, seismic facies 2-1 was observed to cover the entire slice of the diapir (Figure 18a). At a depth of 700 ms TWT, a small portion of 2-1 was observed in the northern part of the diapir while the rest was covered by 2-2 (Figure 18b). At a depth of 1550 ms TWT, the diapir appeared to be half covered by 1-1 in the West and half covered by 1-2 in the East (Figure 18c). At a depth of 1850 ms TWT, it was observed that seismic facies 1-2 covered the entire slice (Figure 18d). Finally, at a depth of 1960 ms TWT, the middle part of the diapir was covered by 2-3 while the remaining areas were covered by 1-2 (Figure 18e).
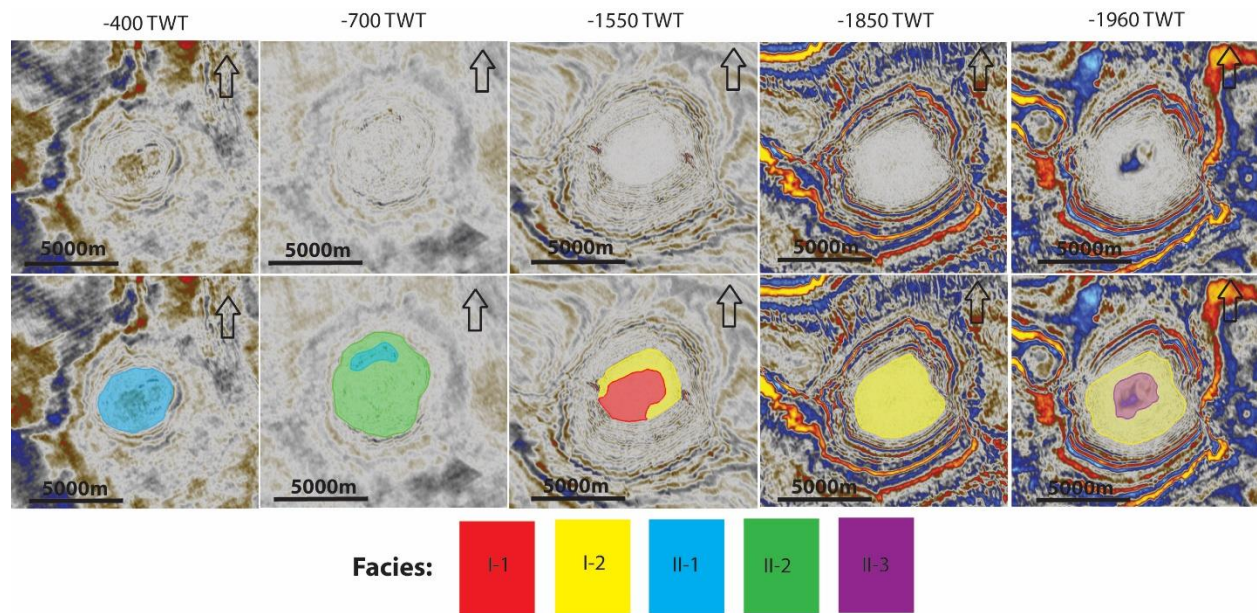
Figure 18: Diamond diapir time-slices before (above) and after (below) interpretation.

For the Ellipsoid diapir, TWT slices were generated at 400 ms, 700 ms, 1550 ms, 1750 ms, and 2150 ms (Figure 19). The results indicated that at a depth of 400 ms TWT, the diapir is predominantly covered by 2-1 in the West, while a small area in the East is covered by 2-2 (Figure 19a). At a depth of 700 ms TWT, the center of the diapir is covered by 2-2, and its edges are covered by 1-2 (Figure 19b). At a depth of 1550 ms TWT, the diapir is mainly covered by 1-1 in the West, and a small portion of it is covered by 1-2 in the East (Figure 19c). At a depth of 1750 ms TWT, a small part of the diapir is covered by 1-1 in the West, and a large part is covered by 1-

2 in the East (Figure 19d). Finally, at a depth of 2150 ms TWT, the whole slice of the diapir is covered by 2-3 (Figure 19e).
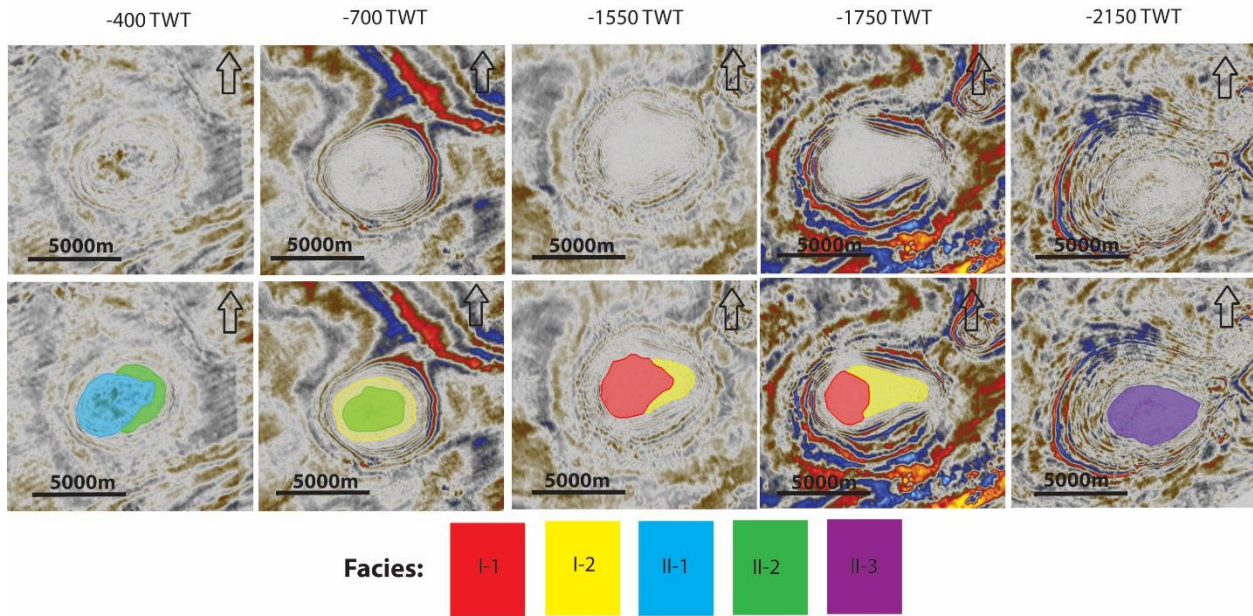
Figure 19: Ellipsoid diapir time-slices before (above) and after (below) interpretation.

5.6. Salt facies from 3D modeling

To obtain a more comprehensive understanding of the internal compositional variations of salt diapirs, 3D models were created for the target diapirs. The first 3D model of the Diamond diapir was obtained through the interpretation of seismic data using the "interpret multi-Z" function in SLB Petrel, resulting in a 3D model covered by multiple lines along both inline and crossline directions (Figure 20a). Interpreted lines were converted to surfaces by generating editable triangle meshes as a 3D plastic model (Figure 20b). In addition, denser seismic time slices at every 200 ms were interpreted to provide a better image of sub-facies inside the salt diapir (Figure 20c).

As observed from the 3D models of the Diamond diapir, the interpreted internal seismic facies II-1 extended from 400 ms to 800 ms. It is followed by seismic facies, II-2, which extended until 1000 ms, where halite-dominated seismic facies I appears. Surrounded by seismic facies I-2, facies I-1 was developed between 1200 ms and 1800 ms. The last anhydrite-dominated seismic facies, II-3, was developed at 2000 ms and extended until the bottom of the salt formation.
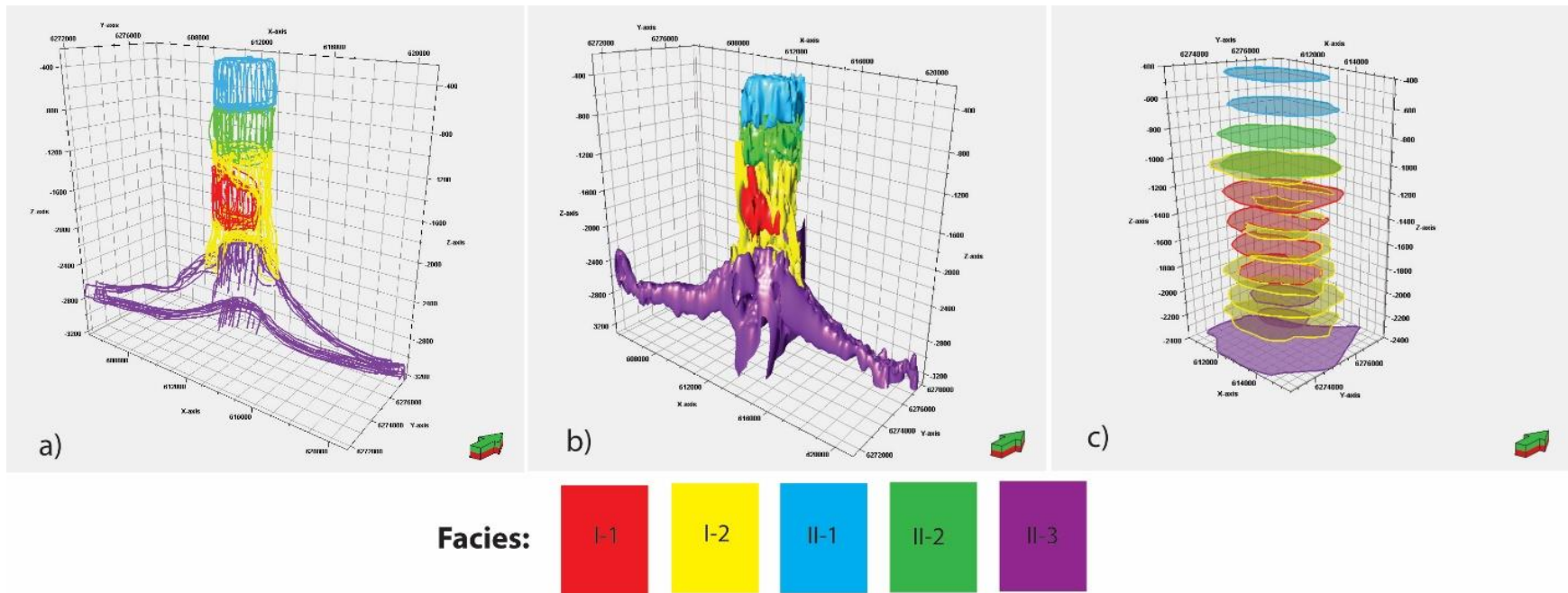
Figure 20: 3D models of the Diamond diapir. (a) 3D line model of the Diamond diapir; (b) 3D plastic model of the Diamond diapir; (c) 3D sliced model of the Diamond diapir.

The same 3D modeling method and workflow were applied to model the Ellipsoid diapir (Figure 21). As shown in the models, the seismic facies II-1 was developed from 200 ms to 600 ms. Beneath seismic facies II-1, facies II-2 extended until 800 ms, where halite-dominated seismic facies started. Surrounded by seismic facies I-2, facies I-1 was developed from 1100 ms to 2000 ms. The last seismic facies, II-3, start at 2200 ms and extended all the way down to the bottom of the salt formation.

Figure 21: 3D models of the Ellipsoid diapir. (a) 3D line model of the Ellipsoid diapir; (b) 3D plastic model of the Ellipsoid diapir; (c) 3D sliced model of the Ellipsoid diapir.

6. Discussion

6.1. Zechstein Group seismic facies in the Norwegian North Sea correlates to depositional cycles in the Netherlands

The interpreted five internal seismic facies observed within the salt diapirs in this study demonstrate significant similarities to the five depositional cycles identified in the Zechstein Group of the Netherlands. Fir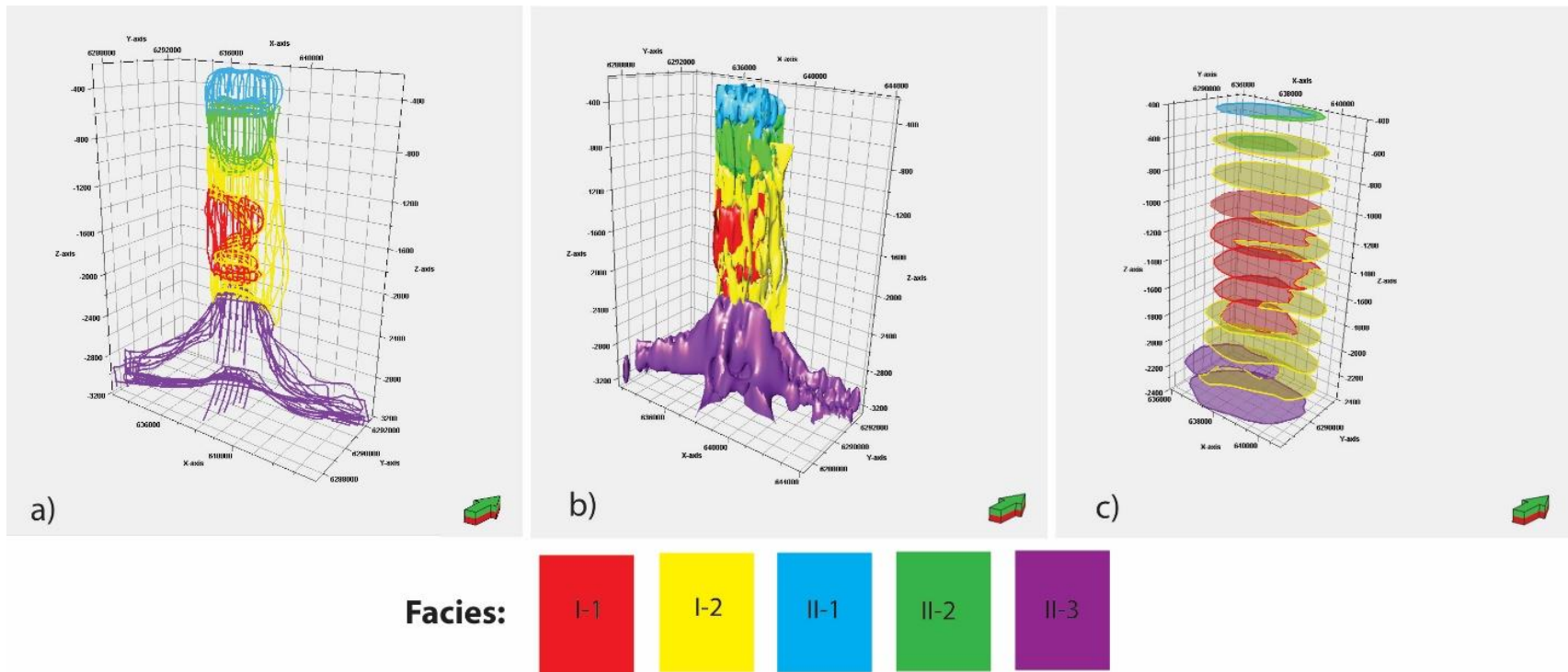st of all, the initial Zechstein cycle Z1 exhibits similarities with the seismic facies II-3 due to their shared composition of anhydrite, shale, and dolomite (Duffy et al., 2023; Pichat, 2022). Additionally, their sequential deposition within the Zechstein Group further supports this correlation. Secondly, the subsequent cycle, Z2, characterized by substantial homogenous halite, aligns with the seismic facies I-1 in terms of both their depositional order and composition (Duffy et al., 2023; Pichat, 2022). Notably, the halite units within Z2 have been utilized in Germany for salt cavern construction, thereby reinforcing the suitability of the seismic facies I-1 as the target facies in this study (Duffy et al., 2023). Moving on to the third cycle, Z3, and the seismic facies I-2, both contain halite units intercalated with claystone and sylvinite (Duffy et al., 2023; Pichat, 2022). Consequently, the seismic facies I-2 can be interpreted as a representation of the Zechstein cycle Z3 in the North Sea region. Lastly, the fourth and fifth cycles, Z4 and Z5, are predominantly composed of anhydrite and occur after halite-dominated cycles (Duffy et al., 2023; Pichat, 2022). Consequently, these cycles can be correlated with the seismic facies II-1 (representation of Z5) and II-2 (representation of Z4), which are considered non-salt cap rock.

6.2. The Potential of CAES in Different Salt Structures

Upon detecting various salt structures within the study area, four primary types were identified: bedded salt layers, salt pillows, salt rollers, and salt diapirs. These structures were thoroughly examined and compared to determine the most suitable reservoir for compressed air energy storage (Table 4). Based on seismic observations, an analysis of the bedded salt layers indicated their possible potential as a viable option due to their relatively clear seismic image and effective lithology control resulting from minimal deformation. However, the narrowness of the halite units poses a challenge in meeting the required height-to-diameter ratio (>0.5). Given the thinness of
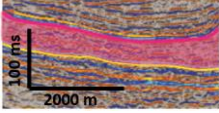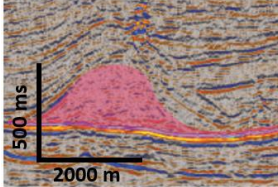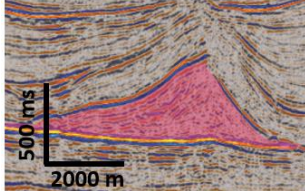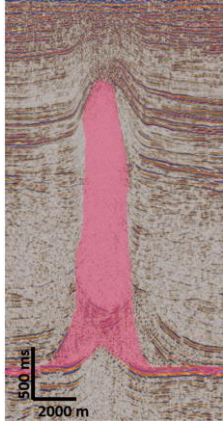
these units, it is likely that interbeds exceed 3 meters in thickness, which can compromise cavern stability. Moreover, uncertainties exist regarding the thickness of the cap rock, and the bedded salt layers are situated at depths greater than 1500 meters, resulting in substantial overburden pressure.

Similarly, salt pillows and salt rollers exhibit favorable characteristics. The thickness of their halite units adequately satisfies the height-to-diameter ratio and allows for the creation of substantial salt caverns. However, these structures also present significant challenges. Although they are not as deep as bedded salt layers, they are generally buried at depths greater than 1500 meters. Additionally, thick interbeds and intercalations are observed, and uncertainties persist regarding the thickness of the cap rock.

In contrast, despite poor seismic imaging due to high deformation, salt diapirs show promise as the most suitable option for a CAES reservoir as observed from the seismic data. They display significant volumes of clean and homogenous seismic reflectors that were interpreted as halite units, those extensive halite units readily satisfy the height-to-diameter ratio and provide ample volumes for cavern creation. Moreover, they seem to be shallower than 1500 meters, enabling the presence of halite beds at shallower depths. It can be inferred that salt diapirs possess halite units with minimal interbeds or even an absence thereof due to the abundance of homogenous halite units. Consequently, salt diapirs emerge as the primary focus of this study.

Table 4: Comparison of salt structures.

	Low Deformation	Medium Deformation		High Deformation
	Bedded Salt	Salt Pillow	Salt Roller	Salt Diapir
Seismic Image				
Advantages	Relatively good seismic image and lithology control due to low deformation	Good height-to-diameter ratio. Halite units are thick enough.	Good height-to-diameter ratio. Halite units are thick enough.	Good height-to-diameter ratio. Halite units are thick enough. Usually shallower than 1500m. No need to check the interbed thickness. Large area.
Disadvantages	Interbeds should not be thicker than 3m. Low height-to-diameter ratio, halite beds can be too narrow. Usually deeper than 1500m. Cap rock thickness should be examined.	Interbeds should not be thicker than 3m. Usually deeper than 1500m. Cap rock thickness should be examined.	Interbeds should not be thicker than 3m. Usually deeper than 1500m. Cap rock thickness should be examined.	Poor seismic image and lithology control due to high deformation. Cap rock thickness should be examined.

6.3. Suitability of Salt Diapirs for CAES Applications

The Diamond diapir and the Ellipsoid diapir, located in the southern region of the study area, have been chosen as the focal points for further investigations due to several advantageous factors. Firstly, they are characterized by being the shallowest diapirs compared to others, suggesting the presence of halite units with lower levels of overburden pressure. Secondly, their positioning within an area where 3D seismic surveys are available enhances the reliability of seismic interpretation. Moreover, they seem to boast the largest volumes of clean and homogenous seismic reflectors which were interpreted as halite, thus providing a greater number of potential cavern options. Lastly, they both possess high-amplitude, continuous, and parallel seismic reflectors at their summits, which can be the necessary non-salt cap rock, as illustrated in Figures 22 and 23.

The investigation of internal compositional variations within the targeted salt diapirs revealed the presence of anhydrite intercalations, occasionally occurring alongside shale and siltstone layers, situated at the summits of both diapirs (Figure 16 & 17, Table 3). These anhydrite-dominated facies potentially serve as the necessary non-salt cap rock. As required for CAES operations, the non-salt cap rock should possess a thickness exceeding 0.33 times the cavern diameter (Table 1). Notably, the anhydrite-dominated facies exhibit sufficient thickness to meet this criterion. Subsequently, the halite-dominated facies (I-1 and I-2) represent the target facies for salt cavern formation. Besides, it is imperative to have a salt cap rock above the cavern, with a thickness exceeding 0.25 times the cavern diameter (Table 1). Consequently, the salt cavern must be created at a certain depth within the halite-dominated facies.
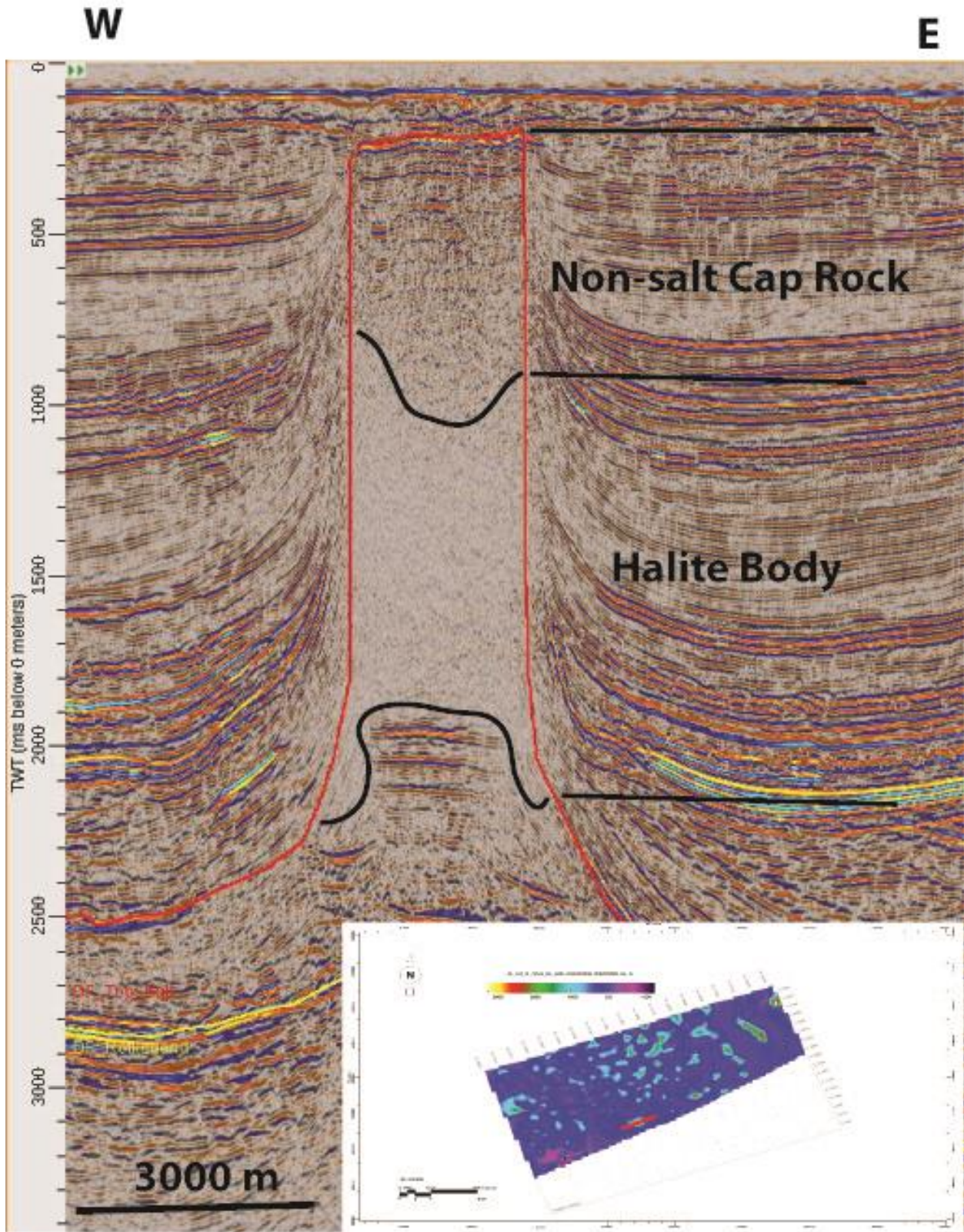
Figure 22: Diamon diapir seismic image.
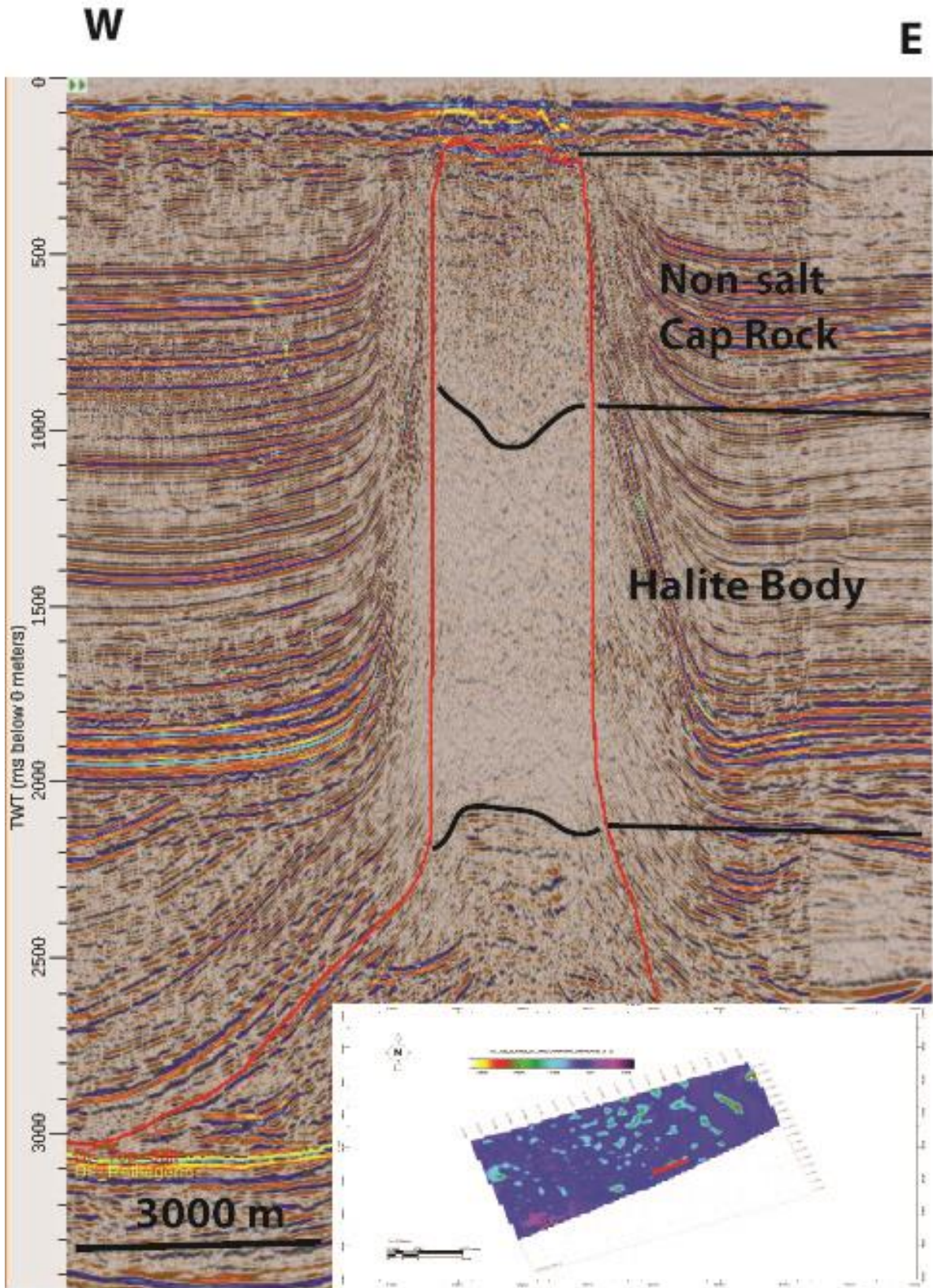
Figure 23: Ellipsoid diapir seismic image.

6.4. Feasibility of CAES in Salt Diapirs

The subsequent step involves calculating the depths of the diapirs and their internal facies. However, it proves exceedingly challenging to perform a direct depth conversion for salt diapirs using computer software due to the considerable difficulties in constructing a velocity model resulting from substantial compositional variations within the diapirs. Consequently, the depth of the diapirs and their internal facies will be manually calculated based on specific assumptions. Seismic velocities associated with distinct rock types will be utilized to convert two-way travel time (TWT) to meters, as outlined in Table 5.

Table 5: Seismic velocities of different rock types (after Kohnen, 1974).

Lithology	Vp (m/s)
Shales	2000-4100
Marine claystone/mudstone	300-1800
Anhydrite	3500-5500
Halite	4000-5500

Conversion from time to depth domain is calculated by the following formula:

$$X = V \times t$$

Where:

X: the distance in meters,

V: the velocity in m/s,

t: the one-way travel time in seconds. It is important to note that TWT values are converted to one-way travel time by dividing it into half.

CAES in the Diamond diapir

The uppermost section of both diapirs is occupied solely by the Nordland Group, characterized by marine claystone. At approximately -200 ms TWT, the summit of the diamond diapir lies buried. According to interpretation, the anhydrite intercalated with shale facies extends to deeper levels, reaching approximately -1000 ms TWT. In this interval, the average velocity of anhydrite and shale will be utilized. Moving further down, the halite-dominated facies, intermittently intercalated with claystone and siltstone (I-2), span from approximately -1000 ms TWT to -1200 ms TWT. In this section, the average velocity of halite and claystone will be used.

As such, the shallowest and the deepest options for different TWT zones are as shown below:

Table 6: Calculation of the shallowest and deepest options for zones in the Diamond diapir.

Zone (ms TWT)	Velocity (m/s)		One-way travel time (s)	Options (m)	
	Shallowest option	deepest option		Shallowest	Deepest
0-200	300	1800	0.1	30	180
200-1000	2750	4800	0.4	1100	1920
1000-1200	2150	3650	0.1	215	365

The depth of the top of the target seismic facies I-1 in the Diamond diapir is:

- The shallowest option: 30 m + 1100 m + 215 m = 1345 m.

- The deepest option: 180 m + 1920 m + 365 m = 2465 m.

Furthermore, these calculations show that the thickness of the non-salt cap rock is 800 m (1100 m – 300 m) for the shallowest option and 1740 m (1920 m – 180 m) for the deepest option. Moreover, the thickness of the salt cap rock, which was interpreted as the seismic facies I-2, is 215 m for the shallowest option and 365 m for the deepest option (Table 7). Either way, the thicknesses of the non-salt cap rock and the salt cap rock are sufficient to create salt caverns beneath them.

Table 7: Thicknesses of the zones in the Diamond diapir.

Overburden	30 m – 180 m
Facies II-1 & II-2	1100 m – 1920 m
Facies I-2	215 m – 365 m

Opting to create a cavern within the homogenous halite (facies I-1) is a safer choice due to the potential stability concerns posed by non-salt interbeds. However, it should be noted that the homogenous halite facies is typically found at greater depths compared to less homogenous halite facies as mentioned before based on the seismic interpretations. Hence, if the homogenous halite

is located at an excessive depth, facies I-2, characterized by halite intercalated with claystone, can be considered as an alternative cavern location.

In the case of the Diamond diapir, if the shallowest option is preferred, a salt cavern can be created within facies I-1, starting from a depth of 1345 meters and extending to 1500 meters. The salt cap rock can be comprised of facies I-2. Based on drilling results, as long as facies I-1 remains shallower than 1500 meters, caverns can be feasibly developed within this facies. However, if facies I-1 surpasses the depth threshold of 1500 meters, facies I-2 should be considered as a more suitable location for the cavern.

CAES in the Ellipsoid diapir

The summit of the ellipsoid diapir is positioned below the Nordland Group and is buried at approximately -200 ms TWT. According to interpretation, the anhydrite intercalated with shale facies extends to deeper levels until approximately -800 ms TWT. Additionally, the halite-dominated facies, occasionally intercalated with claystone and siltstone (I-2), span from approximately -800 ms TWT to -1100 ms TWT.

As such, the shallowest and the deepest options for different TWT zones are as shown below:

Table 8: Calculation of the shallowest and deepest options for zones in the Ellipsoid diapir.

Zone (ms TWT)	Velocity (m/s)		One-way travel time (s)	Options (m)	
	Shallowest option	deepest option		Shallowest	Deepest
0-200	300	1800	0.1	30	180
200-800	2750	4800	0.3	825	1440
800-1100	2150	3650	0.15	323	548

The depth of the top of the target seismic facies I-1 in the Ellipsoid diapir:

- The shallowest option: 30m + 825m + 323m = 1178 m.
- The deepest option: 180m + 1440m + 548m = 2168 m.

Furthermore, these calculations show that the thickness of the non-salt cap rock is 795 m (825 – 30) for the shallowest option and 1260 m (1440 – 180) for the deepest option. Moreover, the thickness of the salt cap rock, which was interpreted as the seismic facies I-2, is 323 m for the shallowest option and 548 m for the deepest option. Either way, the thicknesses of the non-salt cap rock and the salt cap rock are sufficient to create salt caverns beneath them.

Table 9: Thicknesses of the zones in the Ellipsoid diapir.

Overburden	30 m – 180 m
Facies II-1 & II-2	825 m – 1440 m
Facies I-2	323 m – 548 m

When considering the shallowest option, it becomes viable to establish a salt cavern within facies I-1, starting at a depth of 1178 meters and extending to 1500 meters. According to the findings from drilling activities, as long as facies I-1 remains at depths shallower than 1500 meters, it is feasible to construct caverns within this particular facies. However, if the depth exceeds 1500 meters, facies I-2 should be regarded as a more suitable location for the cavern.

6.5. Volumetric Calculations for Caverns in Salt Diapirs

Time-slice sections of both diapirs, corresponding to the initiation of the homogenous halite facies I-1, at respective depths of -1200 ms TWT for the diamond diapir and -1100 ms TWT for the ellipsoid diapir, were extracted for the purpose of calculating the potential volume of a salt cavern, considering the shallowest option (see Figure 24).
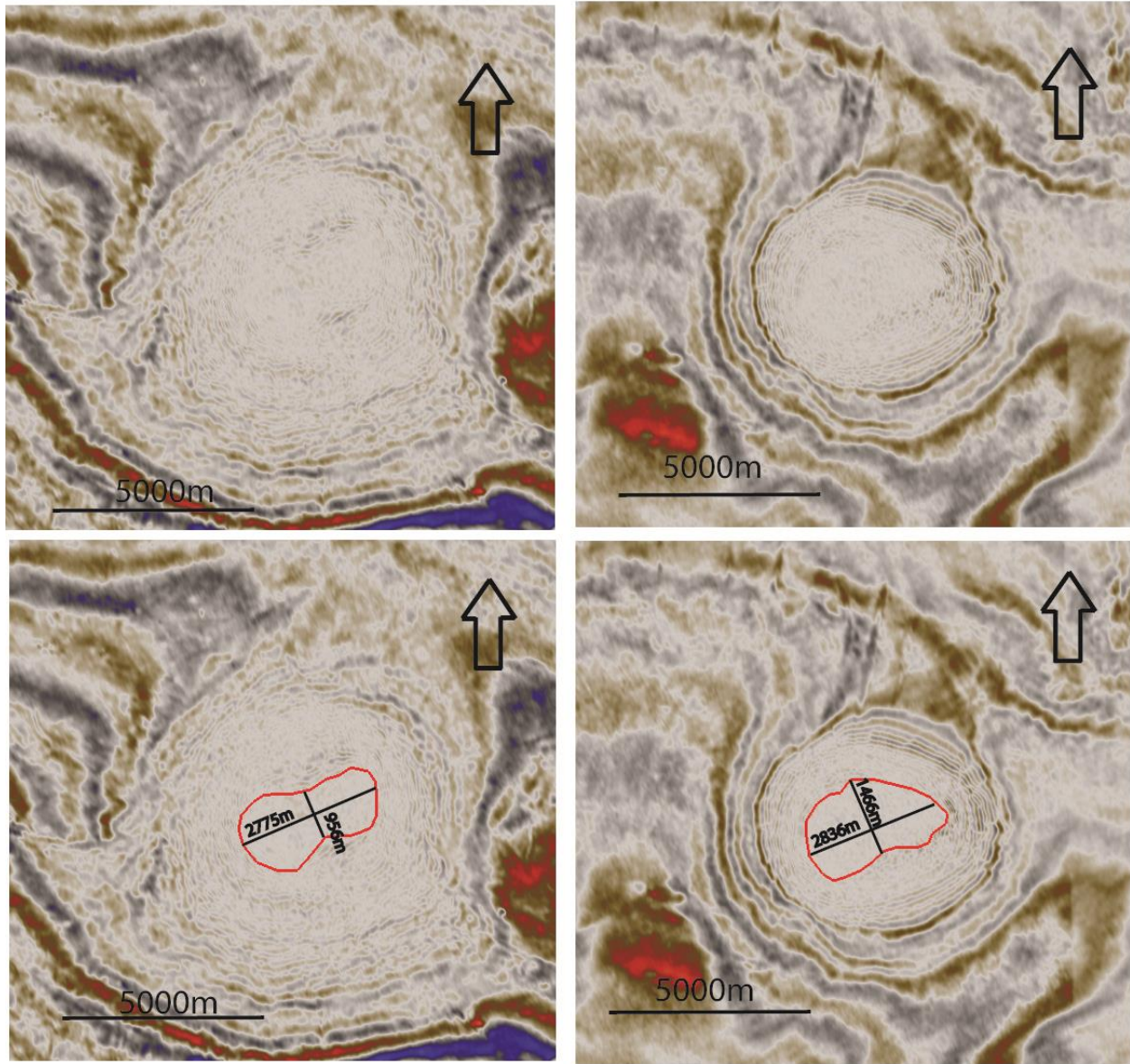
Figure 24: Homogenous halite areas of the target diapirs.

The volume of the possible cavern will be calculated by assuming that the homogenous halite volume is an ellipsoid as below:

$$V = \frac{4}{3} \times \pi \times a \times b \times c$$

Where *a*, *b*, and *c* are the dimensions of the ellipsoid.

The calculated cavern volumes of the Diamond and Ellipsoid diapirs are 11.72 km³ and 5.61 km³, respectively (Table 10).

Table 10: Calculated cavern volumes of the salt diapirs.

Diapir	a (m)	b (m)	c (m)	V (km³)
Diamond	2775	956	155	11.72
Ellipsoid	2836	1466	322	5.61

The output of the Huntorf CAES plant in Germany is 290 MW with a total cavern volume of 310 000 m³, which makes 0.00031 km³. The output of the McIntosh CAES plant in the USA is 110 MW with a total cavern volume of 530 000 m³, which makes 0.00053 km³ (Fjellestad Heitmann, 2020). This indicates that the volumes calculated in this study are sufficient for CAES applications.

6.6. Planning of Salt Cavern Construction

The determined volumes can be occupied by either a solitary cavern or through the creation of multiple caverns. In the event of multiple caverns, it is essential to bear in mind that the spacing between the caverns must exceed three times the diameter of the initial salt cavern.

As a reference, the maximum salt cavern diameter of the Huntorf CAES plant in Germany is 60 meters (Crotogino et al., 2001). Hence, multiple salt caverns with a diameter of 50 meters can be constructed within the Diamond diapir and the Ellipsoid diapir at specific depths: 1345 meters (-1200 ms in TWT) and 1178 meters (-1100 ms in TWT), respectively. Adhering to the geological requirements to construct salt caverns, the spacing between the caverns should exceed 150 meters to accommodate the 50-meter diameter. Furthermore, the non-salt cap rock thickness should surpass 16.5 meters, while the salt cap rock thickness should exceed 12.5 meters. To meet the necessary height-to-diameter ratio (0.5) for the cavern, the salt cavern's height should be more than 25 meters, considering the cavern's 50-meter diameter. However, it is not necessary to limit the cavern's height to 25 meters since it can be constructed to a depth of 1500 meters. In this case, the height of the cavern can be 155 meters for the Diamond diapir and 322 meters for the Ellipsoid diapir (Tables 7 & 9). According to the aforementioned calculations, both salt diapirs fulfill these criteria, with the shallowest option being considered. A bird's eye view (Figure 25) and a cross-

section view (Figure 26) depict the intended salt cavern construction (Illustrated as pink ellipsoid/circle) in the target diapirs, based on the shallowest option.
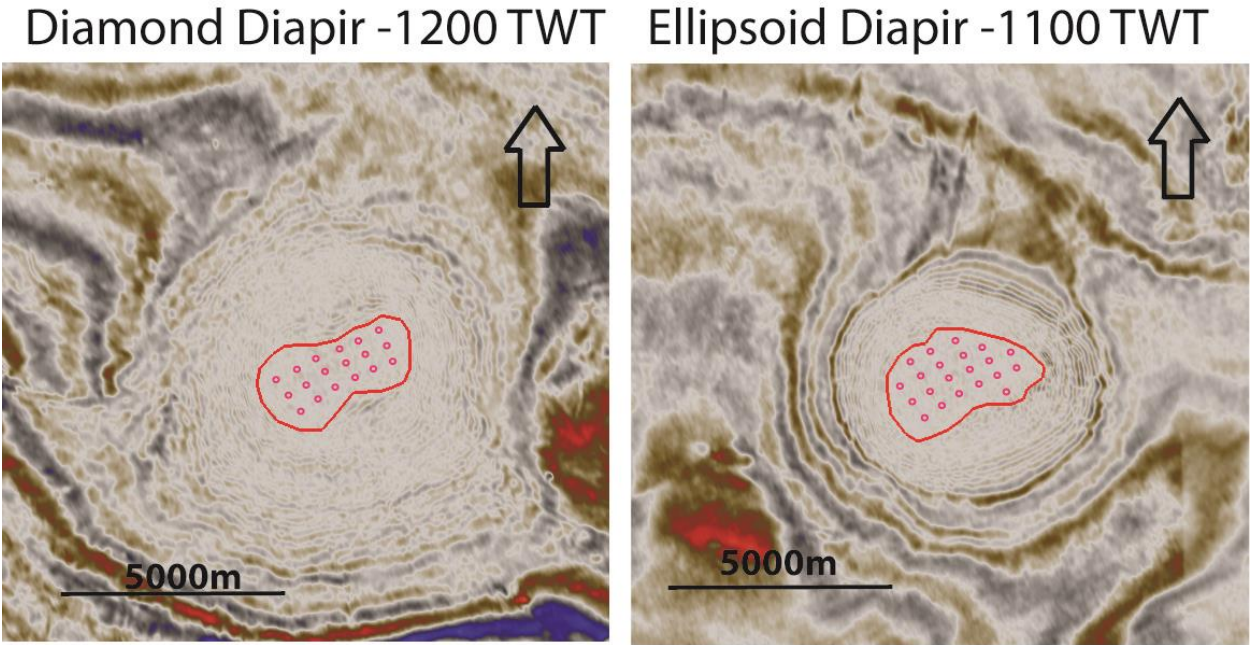
Figure 25: Planned cavern construction for both salt diapirs in a bird's view.
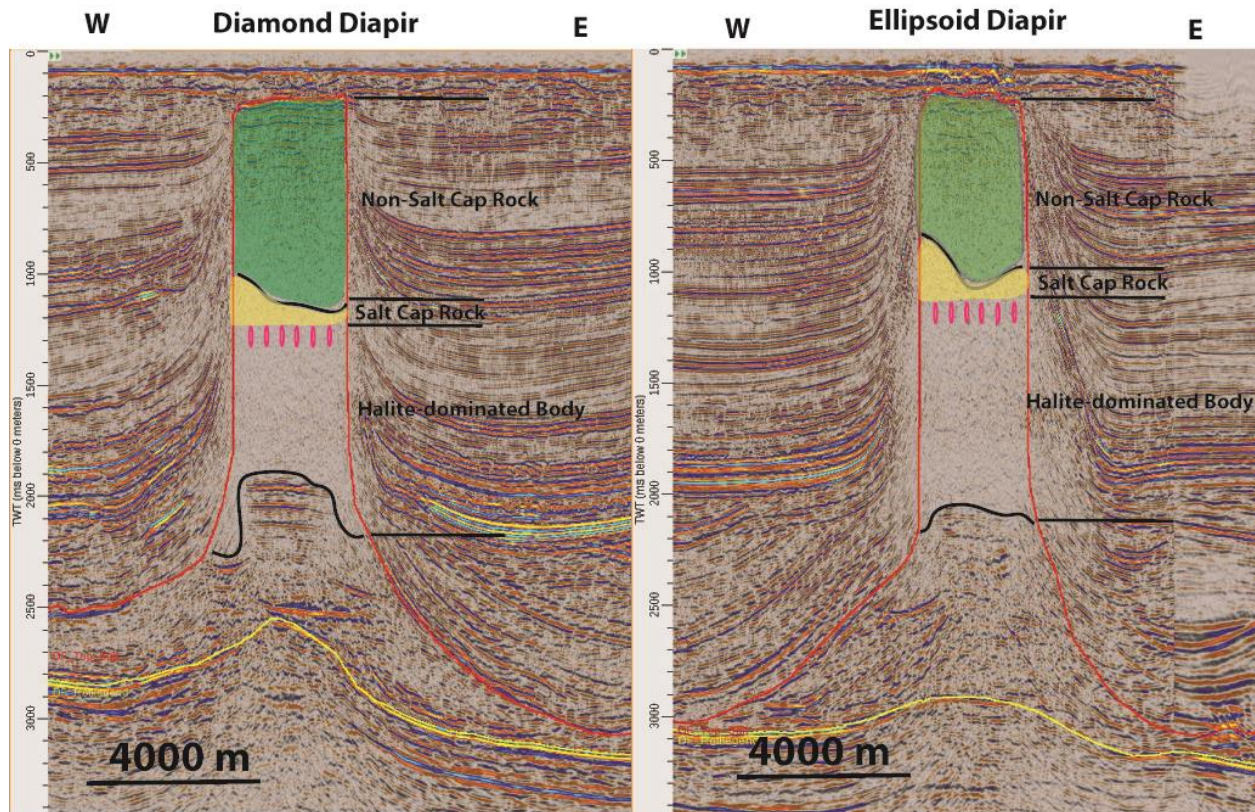
Figure 26: Planned cavern construction for both diapirs in a cross-section view.

7. Conclusions

This study focused on the comprehensive examination, characterization, and discussion of the salt formations and their internal compositions within the Zechstein Group in the Norwegian sector of the southern North Sea. Through the utilization of seismic data interpretation, the creation and interpretation of surface and thickness maps of the salt formations, and the analysis of well logs, reports, and conventional cores, significant findings have been obtained. The outcomes of this study have consequently yielded the following discernible conclusions.

- Four primary salt structure types are observed and interpreted in the study area, including bedded salt layers, salt pillows, salt rollers, and salt diapirs.
- Among these salt structure types, salt diapirs are the most promising options to be a CAES reservoir due to their suitable depth and sufficient volumes of salt bodies.
- Structural maps for the tops of the Rotliegend Group and the Zechstein Group and the thickness map of the Zechstein Group were produced. These maps set the foundation for

51

presenting the localities of different salt structure types and defining favorable diapirs for the CAES operations.

- Two salt diapirs, namely Diamond diapir and Ellipsoid diapir, are proposed for the CAES operations.

- Two main seismic facies and five sub-facies were classified to understand the internal structures of salt diapirs. These facies and sub-facies show significant similarities to five depositional cycles (Z1-Z5) identified in the Zechstein Group of the Netherlands. Anhydrite-dominated facies at the summits of salt diapirs in this study area can correlate to the Dutch Z4 and Z5 depositional cycles of the Zechstein Group. These facies exhibit the potential to serve as non-salt cap rocks for salt caverns.

- Whereas extensive halite-dominated facies may link to the Z2 and Z3 depositional cycles. These facies exhibit the potential to serve as reservoirs for the formation of salt caverns. However, it is essential to utilize certain portions of the halite-dominated facies as salt cap rocks to ensure the structural integrity and containment of the cavern.

- The geological requirements for constructing salt caverns are evaluated. Homogenous halite facies, that is safer to construct salt caverns, are lies buried at a depth of 1345 meters for the Diamond diapir and at a depth of 1178 meters for the Ellipsoid diapir in the most optimistic case. Salt caverns can be constructed up to a depth of 1500 meters to avoid too much overburden pressure.

- The feasibility of CAES in salt diapirs is assessed. Non-salt rock thickness for the Diamond and Ellipsoid diapirs is calculated for both the shallowest and the deepest options. It showed sufficient non-salt cap rock thicknesses to build salt caverns below either way. In addition, salt cap rock thickness for both diapirs was calculated, which presented sufficient salt cap rock thicknesses to build salt caverns below either way.

- The total volumes of salt caverns in the Diamond and Ellipsoid diapirs were calculated, which are 11.722 km^3 and 5.607 km^3, respectively. Compared to the Huntorf CAES plant in Germany and the McIntosh CAES plant in the USA, calculated volumes in this study are sufficient for the CAES applications in the study area.

- Multiple salt caverns with a diameter of 50 meters can be constructed within the Diamond diapir and the Ellipsoid diapir at specific depths: 1345 meters and 1178 meters, respectively. To meet the necessary height-to-diameter ratio (0.5) for the cavern, the salt

52

cavern's height should be more than 25 meters, considering the cavern's 50-meter diameter.

8. Further work

- A promising diapir was identified in the northeastern region of the study area; however, due to the unavailability of a 3D survey in that specific area, a comprehensive interpretation of this diapir is currently hindered. Furthermore, the limited availability of 2D seismic data in the region further highlights the need for a comprehensive seismic data acquisition, particularly in the northeastern part of the study area. Therefore, it is crucial to prioritize the completion of seismic data acquisition, specifically in the northeastern region, to address these limitations and enhance the overall understanding of the area.

- In order to achieve a comprehensive understanding of the internal compositional variations within the target diapirs, it is beneficial to apply several attribute analyses on the 3D seismic cube, such as the spectral decomposition method and other stratigraphic methods. In addition, core sample interpretations were done based only on core sample pictures in this study. Therefore, a fully physical core sample analysis of the adjacent wells outside the study area would be beneficial to understand the internal compositional variations within the salt structures. Furthermore, it has been observed that certain nearby reference wells exhibit local and thin K-Mg salt occurrences, which may pose challenges in terms of drilling and cavern stability. Thus, emphasizing the need for diligent investigation of K-Mg salt presence within the target diapirs through a full core sample analysis.

- Localized areas displaying high-amplitude anomalies were detected at the periphery of the diamond diapir, as depicted in Figure 27. These high-amplitude anomalies potentially signify the presence of hydrocarbons, as the salt body itself can serve as a lateral seal for such resources. Therefore, it is highly recommended to examine the presence of a potential source rock in the region and thoroughly examine this area by opening a drilling well to further investigate the potential hydrocarbon reservoirs.
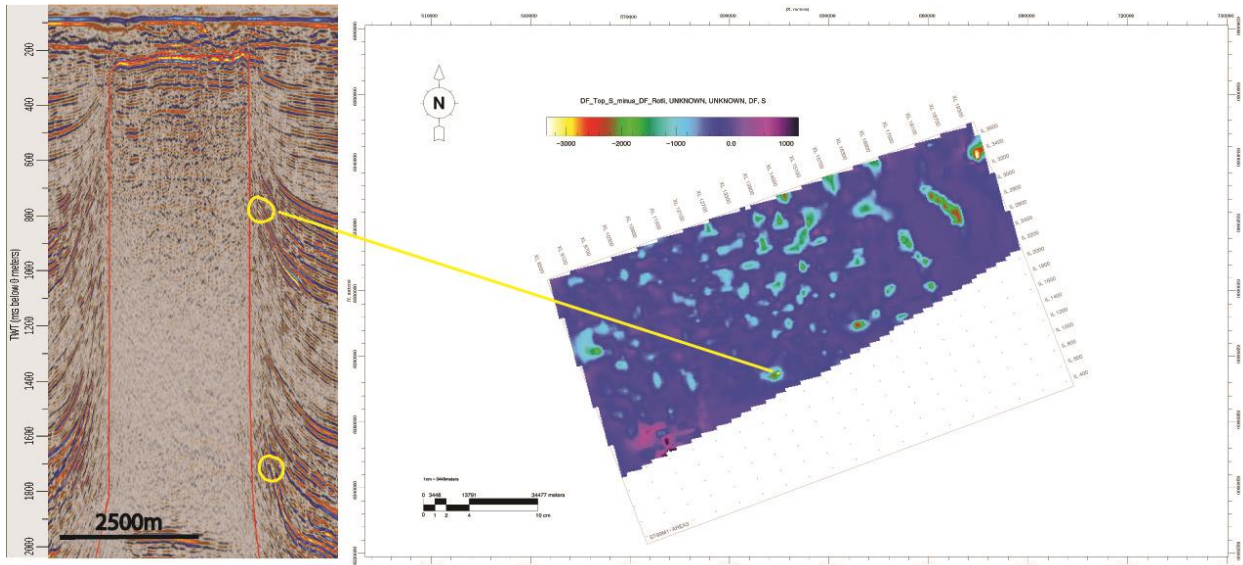
Figure 27: Possible bright spot in the area.

- An extensive and highly promising salt wall, identified in the eastern region of the study area (Figure 28), has captured attention. Nevertheless, the interpretation of its internal seismic facies presents considerable challenges due to its complex nature, and its voluminous dimensions further compound the difficulty. As a result, a more extensive examination of the salt wall, specifically pertaining to its suitability for CAES operations, necessitates a substantial investment of time and resources. Therefore, a future study may focus on the characterization of this salt wall.
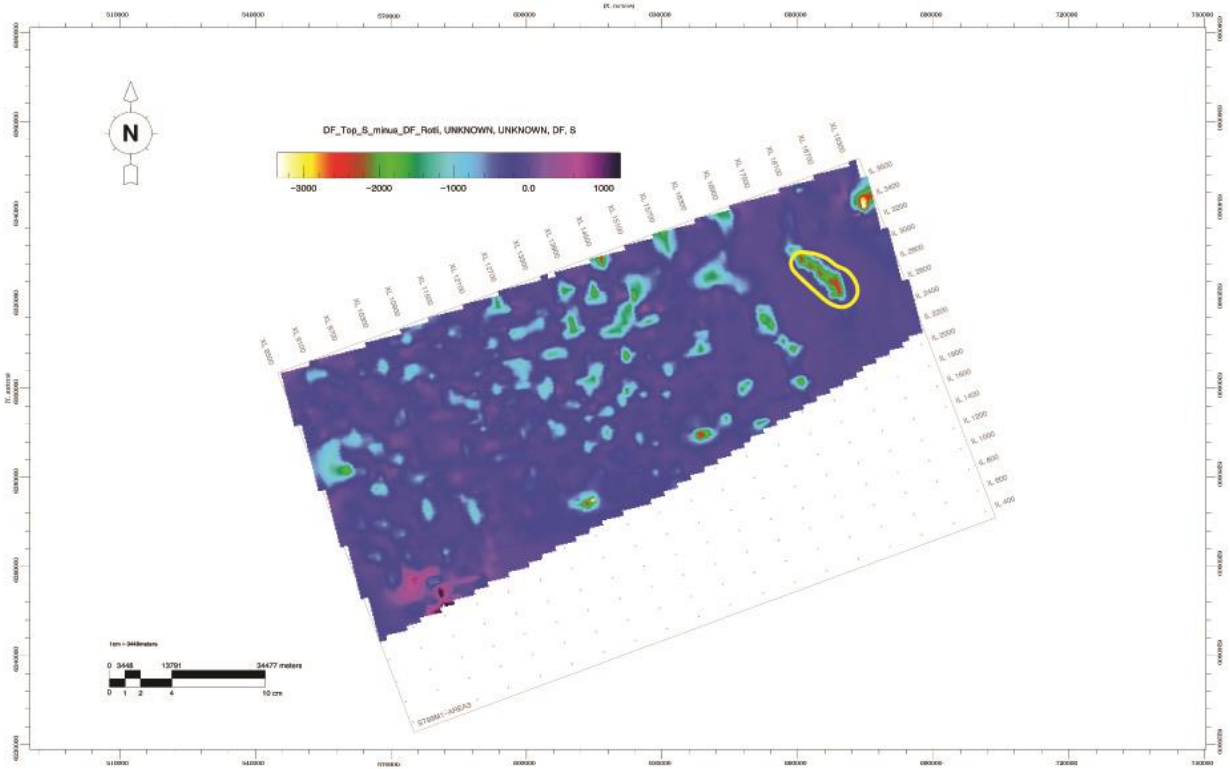
Figure 28: Location of the salt wall in the study area.

References

Abdalla, A. N., Nazir, M. S., Tao, H., Cao, S., Ji, R., Jiang, M., & Yao, L. (2021). Integration of energy storage system and renewable energy sources based on Artificial Intelligence: An overview. *Journal of Energy Storage*, *40*, 102811.

Amrouche, S. O., Rekioua, D., & Rekioua, T. (2015). Overview of energy storage in renewable energy systems. *2015 3rd International Renewable and Sustainable Energy Conference (IRSEC)*.

Arsad, A. Z., Hannan, M. A., Al-Shetwi, A. Q., Mansur, M., Muttaqi, K. M., Dong, Z. Y., & Blaabjerg, F. (2022). Hydrogen Energy Storage Integrated Hybrid Renewable Energy Systems: A review analysis for Future Research Directions. *International Journal of Hydrogen Energy*, *47*(39), 17285–17312.

Ball, M., & Weeda, M. (2015). The hydrogen economy—vision or reality? *Compendium of Hydrogen Energy*, 237–266.

Barton, J. P., & Infield, D. G. (2004). Energy storage and its use with intermittent renewable energy. *IEEE Transactions on Energy Conversion*, *19*(2), 441–448.

Bocklisch, T. (2015). Hybrid Energy Storage Systems for Renewable Energy Applications. *Energy Procedia*, *73*, 103–111.

Borri, E., Tafone, A., Comodi, G., Romagnoli, A., & Cabeza, L. F. (2022). Compressed air energy storage—an overview of research trends and gaps through a bibliometric analysis. *Energies*, *15*(20), 7692.

Bünger, U., Michalski, J., Crotogino, F., & Kruck, O. (2016). Large-scale underground storage of hydrogen for the grid integration of renewable energy and other applications. *Compendium of Hydrogen Energy*, 133–163.

Caglayan, D. G., Weber, N., Heinrichs, H. U., Linßen, J., Robinius, M., Kukla, P. A., & Stolten, D. (2020). Technical potential of salt caverns for hydrogen storage in Europe. *International Journal of Hydrogen Energy*, *45*(11), 6793–6805.

Connolly, D., Lund, H., Mathiesen, B. V., Pican, E., & Leahy, M. (2012). The technical and economic implications of integrating fluctuating renewable energy using energy storage. *Renewable Energy*, *43*, 47–60.

Crotogino, F., Mohmeyer, K.-U., & Scharf, R. (2001). *Huntorf CAES: More than 20 Years of Successful Operation*.

Crotogino, F., Schneider, G.-S., & Evans, D. J. (2017). Renewable energy storage in geological formations. *Proceedings of the Institution of Mechanical Engineers, Part A: Journal of Power and Energy*, *232*(1), 100–114.

DeCarolis, J. F., & Keith, D. W. (2006). The economics of large-scale wind power in a carbon constrained world. *Energy Policy*, *34*(4), 395–410.

Donadei, S., & Schneider, G.-S. (2022). Compressed Air Energy Storage. *Storing Energy*, 141–156.

Duffy, O., Hudec, M., Peel, F., Apps, G., Bump, A., Moscardelli, L., Dooley, T., Bhattacharya, S., Wisian, K., & Shuster, M. (2022). *The Role of Salt Tectonics in the Energy Transition: An Overview and Future Challenges*.

Duhan, J. (2018). *Compressed Air Energy Storage in Salt Caverns: Geomechanical Design Workflow, CAES Siting Study from a Geomechanics Perspective, and Deep Brine Disposal (Master's Thesis, University of Waterloo)*.

Evans, D., Parkes, D., Dooner, M., Williamson, P., Williams, J., Busby, J., He, W., Wang, J., & Garvey, S. (2021). Salt Cavern Exergy Storage capacity potential of UK massively bedded Halites, using compressed air energy storage (CAES). *Applied Sciences*, *11*(11), 4728.

Evans, D., Stephenson, M., & Shaw, R. (2009). The present and future use of 'land' below ground. *Land Use Policy*, *26*.

Feldmann, F., Hagemann, B., Ganzer, L., & Panfilov, M. (2016). Numerical simulation of hydrodynamic and gas mixing processes in underground hydrogen storages. *Environmental Earth Sciences*, *75*(16).

Fırseth, R. B., Knudsen, B.-E., Liljedahl, T., Midbøe, P. S., & Søderstrøm, B. (1997). Oblique rifting and sequential faulting in the Jurassic development of the northern North Sea. *Journal of Structural Geology*, *19*(10), 1285–1302.

Gasanzade, F., Witte, F., Tuschy, I., & Bauer, S. (2023). Integration of geological compressed air energy storage into future energy supply systems dominated by renewable power sources. *Energy Conversion and Management*, *277*, 116643.

Geissbühler, L., Becattini, V., Zanganeh, G., Zavattoni, S., Barbato, M., Haselbacher, A., & Steinfeld, A. (2018). Pilot-scale demonstration of advanced adiabatic compressed air energy storage, part 1: Plant description and tests with sensible thermal-energy storage. *Journal of Energy Storage*, *17*, 129–139.

Gillhaus, A., & Horvath, P. L. (2008). Compilation of geological and geotechnical data of worldwide domal salt deposits and domal salt cavern fields. *Solution Mining Research Insitute and KBB Underground Technologies GmbH, Clarks Summit, PA, USA*.

Gérard, J., & Buhrig, C. (1990). Seismic facies of the Permian section of the Barents Shelf: Analysis and interpretation. *Marine and Petroleum Geology*, *7*(3), 234–252.

Glennie, K. W., Collinson, J. D., Evans, D. J., Holliday, D. W., & Jones, N. S. (2005). *Carboniferous Hydrocarbon Resources: The Southern North Sea and Surrounding Areas*.

Hamilton, E. L. (1971). Elastic properties of marine sediments. *Journal of Geophysical Research*, *76*(2), 579–604.

He, Y., Guo, S., Zhou, J., Song, G., Kurban, A., & Wang, H. (2022). The multi-stage framework for optimal sizing and operation of hybrid electrical-thermal energy storage system. *Energy*, *245*, 123248.

Heitmann, M. F. (2020). *Modelling and Evaluating of Compressed Air Energy Storage System (Master's Thesis, University of South-Eastern Norway)*.

Ibrahim, H., Ilinca, A., & Perron, J. (2008). Energy Storage Systems—characteristics and comparisons. *Renewable and Sustainable Energy Reviews*, *12*(5), 1221–1250.

Jackson, C. A.-L., & Stewart, S. A. (2017). Composition, tectonics, and hydrocarbon significance of Zechstein supergroup salt on the United Kingdom and Norwegian Continental shelves. *Permo-Triassic Salt Provinces of Europe, North Africa and the Atlantic Margins*, 175–201.

Jackson, M. P. A., & Talbot, C. J. (1986). External shapes, strain rates, and dynamics of salt structures. *Geological Society of America Bulletin*, *97*(3), 305.

Jackson, M. P., & Hudec, M. R. (2017). *Salt Tectonics: Principles and Practice. Cambridge University Press*.

Jafarizadeh, H., Soltani, M., & Nathwani, J. (2020). Assessment of the HUNTORF compressed air energy storage plant performance under enhanced modifications. *Energy Conversion and Management*, *209*, 112662.

Karlo, J. F., van Buchem, F. S., Moen, J., & Milroy, K. (2014). Triassic-age salt tectonics of the central North Sea. *Interpretation*, *2*(4).

Kebede, A. A., Kalogiannis, T., Van Mierlo, J., & Berecibar, M. (2022). A comprehensive review of stationary energy storage devices for large scale renewable energy sources grid integration. *Renewable and Sustainable Energy Reviews*, *159*, 112213.

Kim, H.-M., Rutqvist, J., Ryu, D.-W., Choi, B.-H., Sunwoo, C., & Song, W.-K. (2012). Exploring the concept of compressed air energy storage (CAES) in lined rock caverns at shallow depth: A modeling study of air tightness and Energy Balance. *Applied Energy*, *92*, 653–667.

Labaune, P., Rouabhi, A., Tijani, M., Blanco-Martín, L., & You, T. (2017). Dilatancy criteria for Salt Cavern Design: A comparison between stress- and strain-based approaches. *Rock Mechanics and Rock Engineering*, *51*(2), 599–611.

Lankof, L., & Tarkowski, R. (2020). Assessment of the potential for underground hydrogen storage in bedded salt formation. *International Journal of Hydrogen Energy*, *45*(38), 19479–19492.

Lankof, L., Urbańczyk, K., & Tarkowski, R. (2022). Assessment of the potential for underground hydrogen storage in salt domes. *Renewable and Sustainable Energy Reviews*, *160*, 112309.

Lewis, M. M., Jackson, C. A.-L., & Gawthorpe, R. L. (2013). Salt-influenced normal fault growth and forced folding: The Stavanger Fault System, North Sea. *Journal of Structural Geology*, *54*, 156–173.

Maia da Costa, A., V. M da Costa, P., D. Udebhulu, O., Cabral Azevedo, R., FF Ebecken, N., CO Miranda, A., … & Breda, A. (2019). Potential of storing gas with high CO2 content in salt caverns built in ultra-deep water in Brazil. *Greenhouse Gases: Science and Technology, 9(1)*, 79–94.

Marín, D., Cardozo, N., & Escalona, A. (2023). Compositional variation of the Zechstein Group in the Norwegian North Sea: Implications for underground storage in Salt Caverns. *Basin Research*.

Matos, C. R., Silva, P. P., & Carneiro, J. F. (2022). Overview of compressed air energy storage projects and regulatory framework for Energy Storage. *Journal of Energy Storage*, *55*, 105862.

Małachowska, A., Łukasik, N., Mioduska, J., & Gębicki, J. (2022). Hydrogen storage in geological formations—the potential of Salt Caverns. *Energies*, *15*(14), 5038.

Melaina, M. W., Antonia, O., & Penev, M. (2013). *Blending Hydrogen into Natural Gas Pipeline Networks: A Review of Key Issues*.

Mlilo, N., Brown, J., & Ahfock, T. (2021). Impact of intermittent renewable energy generation penetration on the Power System Networks – A Review. *Technology and Economics of Smart Grids and Sustainable Energy*, *6*(1).

Mongird, K., Viswanathan, V., Balducci, P., Alam, J., Fotedar, V., Koritarov, V., & Hadjerioua, B. (2019). *Energy Storage Technology and Cost Characterization Report*.

Mueller, E., Greplowski, Z., & Stuberg, L. (2019). Zechstein salt canopies, Jæren High, Norwegian North Sea – triassic subsalt play potential. *81st EAGE Conference and Exhibition 2019*.

Olabi, A. G. (2017). Renewable Energy and Energy Storage Systems. *Energy*, *136*, 1–6.

Oljedirektoratet. (n.d.). https://www.npd.no/

Osagiede, E. E., Rotevatn, A., Gawthorpe, R., Kristensen, T. B., Jackson, C. A.-L., & Marsh, N. (2020). Pre-existing intra-basement shear zones influence growth and geometry of non-colinear normal faults, western utsira high–Heimdal Terrace, North Sea. *Journal of Structural Geology*, *130*, 103908.

Ozarslan, A. (2012). Large-scale hydrogen energy storage in Salt Caverns. *International Journal of Hydrogen Energy*, *37*(19), 14265–14277.

Panfilov, M. (2016). Underground and pipeline hydrogen storage. *Compendium of Hydrogen Energy*, 91–115.

Parkes, D., Evans, D. J., Williamson, P., & Williams, J. D. O. (2018). Estimating available salt volume for potential CAES development: A case study using the northwich halite of the Cheshire Basin. *Journal of Energy Storage*, *18*, 50–61.

Pichat, A. (2022). Stratigraphy, paleogeography and depositional setting of the K–mg salts in the Zechstein Group of netherlands—implications for the development of Salt Caverns. *Minerals*, *12*(4), 486.

Ravestein, P., van der Schrier, G., Haarsma, R., Scheele, R., & van den Broek, M. (2018). Vulnerability of European intermittent renewable energy supply to climate change and climate variability. *Renewable and Sustainable Energy Reviews*, *97*, 497–508.

Reddy Salkuti, S., & Mook Jung, C. (2018). Comparative analysis of storage techniques for a grid with renewable energy sources. *International Journal of Engineering & Technology*, *7*(3), 970.

Rojo, L. A., Cardozo, N., Escalona, A., & Koyi, H. (2019). Structural style and evolution of the Nordkapp Basin, Norwegian Barents Sea. *AAPG Bulletin*, *103*(9), 2177–2217.

Rojo, L. A., Koyi, H., Cardozo, N., & Escalona, A. (2020). Salt tectonics in salt-bearing rift basins: Progradational loading vs extension. *Journal of Structural Geology*, *141*, 104193.

Rossland, A., Escalona, A., & Rolfsen, R. (2013). Permian–holocene tectonostratigraphic evolution of the Mandal High, Central Graben, North Sea. *AAPG Bulletin*, *97*(6), 923–957.

Rowan, M. G., Urai, J. L., Fiduk, J. C., & Kukla, P. A. (2019). Deformation of intrasalt competent layers in different modes of salt tectonics. *Solid Earth*, *10*(3), 987–1013.

Sadeghi, S., Ghandehariun, S., Rezaie, B., & Javani, N. (2021). *An Innovative Solar-Assisted Compressed Air Energy Storage System Integrated with a Liquefied Air Power Cycle*.

Schultz-Ela, D. D., Jackson, M. P. A., & Vendeville, B. C. (1993). Mechanics of Active Salt Diapirism. *Tectonophysics*, *228*(3–4), 275–312.

Stewart, S. A. (2007). Salt tectonics in the North Sea Basin: A structural style template for seismic interpreters. *Geological Society, London, Special Publications*, *272*(1), 361–396.

Stone, H. B., Veldhuis, I., & Richardson, R. N. (2009). Underground hydrogen storage in the UK. *Geological Society, London, Special Publications*, *313*(1), 217–226.

Succar, S., & Williams, R. H. (2008). Compressed air energy storage: theory, resources, and applications for wind power. *Princeton Environmental Institute Report*, *8*, 81.

Sørensen, S., Morizot, H., & Skottheim, S. (1992). A tectonostratigraphic analysis of the southeast Norwegian North Sea Basin. *Structural and Tectonic Modelling and Its Application to Petroleum Geology*, 19–42.

Tarkowski, R. (2019). Underground hydrogen storage: Characteristics and prospects. *Renewable and Sustainable Energy Reviews*, *105*, 86–94.

The Millennium Atlas Petroleum Geology of the Central and northern North Sea. (2003). The Geological Society of London.

United Nations. (n.d.). https://www.un.org/

Wang, Z., Carriveau, R., Ting, D. S. -K., Xiong, W., & Wang, Z. (2019). A review of Marine Renewable Energy Storage. *International Journal of Energy Research*, *43*(12), 6108–6150.

Wicker, V., & Ford, M. (2021). Assessment of the tectonic role of the Triassic evaporites in the north Toulon fold-thrust belt. *BSGF - Earth Sciences Bulletin*, *192*, 51.

Wu, Z., Yin, H., Wang, X., Zhao, B., Zheng, J., Wang, X., & Wang, W. (2015). The structural styles and formation mechanism of salt structures in the southern Precaspian Basin: Insights from seismic data and analog modeling. *Marine and Petroleum Geology*, *62*, 58–76.

Yartys, V. A., & Lototsky, M. V. (2004). An overview of hydrogen storage methods. *Hydrogen Materials Science and Chemistry of Carbon Nanomaterials*, 75–104.

Zhou, L. (2004). Progress and problems in hydrogen storage methods. *Renewable and Sustainable Energy Reviews*, *9*(4), 395–408.

Ziegler, P. A., & Hoorn, B. van. (1989). Evolution of north sea rift system. *Extensional Tectonics and Stratigraphy of the North Atlantic Margins*.